

# ANATOMY OF THE BAR INSTABILITY IN CUSPY DARK MATTER HALOS

JOHN DUBINSKI<sup>1</sup>, INGO BERENTZEN<sup>2</sup> AND ISAAC SHLOSMAN<sup>3,4</sup>

*Draft version December 28, 2018*

## ABSTRACT

We examine the bar instability in galactic models with an exponential disk and a cuspy dark matter (DM) halo with a Navarro-Frenk-White (NFW) cosmological density profile. The equilibrium models are constructed from a 3-integral composite distribution function but subject to the bar instability. We generate a sequence of models with a range of mass resolution from 1.8K to 18M particles in the disk and 10K to 100M particles in the halo along with a multi-mass model with an effective resolution of  $\sim 10^{10}$  particles. We describe how mass resolution affects the bar instability, including its linear growth phase, the buckling instability, pattern speed decay through the resonant transfer of angular momentum to the DM halo, and the possible destruction of the halo cusp. Our higher resolution simulations show a converging spectrum of discrete resonance interactions between the bar and DM halo orbits. As the pattern speed decays, orbital resonances sweep through most of the DM halo phase space and widely distribute angular momentum among the halo particles. The halo does not develop a flat density core and preserves the cusp, except in the region dominated by gravitational softening. The formation of the bar increases the central stellar density and the DM is compressed adiabatically increasing the halo central density by  $1.7\times$ . Overall, the evolution of the bar displays a convergent behavior for halo particle numbers between 1M and 10M particles, when comparing bar growth, pattern speed evolution, the DM halo density profile and a nonlinear analysis of the orbital resonances. Higher resolution simulations clearly illustrate the importance of discrete resonances in transporting the angular momentum from the bar to the halo.

*Subject headings:* galaxies: structure — galaxies: evolution — galaxies: kinematics and dynamics — methods: N-body simulations — cosmology: dark matter

## 1. INTRODUCTION

More than 2/3 of disk galaxies host stellar bars (e.g., Knapen et al. 2000; Grosbøl et al. 2004; Marinova & Jogee 2007) and evolution of this fraction with redshift is a matter of an ongoing debate (e.g., Jogee et al. 2004; Sheth et al. 2008). Numerical simulations of disk galaxies have shown that bars form either as a result of a global gravitational instability (e.g., Toomre 1981; Sellwood & Wilkinson 1993) or they are triggered by galaxy interactions (e.g., Byrd et al. 1986; Noguchi 1987) and interactions with DM substructure (e.g., Gauthier et al. 2006; Dubinski et al. 2008; Romano-Diaz et al. 2008). A large body of theoretical work on the bar instability has examined the properties of bars that emerge in initially unstable disks in  $N$ -body simulations. While these experiments explore an idealized picture of bar formation, they reveal important aspects of the phenomenology of the bar instability, including bar growth within the corotation (CR) radius, the vertical buckling instability, and the transport of angular momentum through gravitational torques from resonant orbits in the outer disk and the surrounding dark matter (DM) halo. The importance of the resonance nature of angular

momentum loss by bars and spirals was first pointed out by Lynden-Bell & Kalnajs (1972). Angular momentum transfer was studied subsequently both in idealized models with rigid bars in live halos (Weinberg 1985; Hernquist & Weinberg 1992; Weinberg & Katz 2002, 2007a); and self-consistent  $N$ -body simulations with bar-unstable disks (e.g., Sellwood 1980; Athanassoula 1996; Debattista & Sellwood 1998; Valenzuela & Klypin 2003; O’Neill & Dubinski 2003), with resonant transfer mechanisms being explored explicitly in some studies (e.g. Athanassoula 2002; Holley-Bockelmann et al. 2005; Martinez-Valpuesta et al. 2006; Ceverino & Klypin 2007). These studies have shown that the halo absorbs angular momentum from the bar that leads to the decline of the bar pattern speed.

Previous results reveal a close connection between numerical bars and observed galactic systems in many structural details, including a link between the peanut-shaped bulges and (buckled) bars (e.g., Combes & Sanders 1981; Combes et al. 1990; Raha et al. 1991; Berentzen et al. 1998; Patsis et al. 2002; Martinez-Valpuesta et al. 2006; Debattista et al. 2006). The observational determination of bar pattern speeds (e.g., Kent 1987; Merrifield & Kuijken 1995; Corsini et al. 2007) suggest that stellar bars are predominantly “fast” (but see Rautiainen et al. (2008) for a different view) meaning that they are near the maximum possible length of the CR radius permitted by the orbital dynamics (Contopoulos 1980; Athanassoula 1992). If evolved for too long, the numerical bars can appear “slow” with lengths significantly shorter than the CR radius and pattern speeds that seem abnormally low when compared to observations of real barred galaxies

<sup>1</sup> Department of Astronomy and Astrophysics, University of Toronto, 50 St. George Street, Toronto, ON M5S 3H4, Canada; dubinski@astro.utoronto.ca

<sup>2</sup> Astronomisches Rechen-Institut, Zentrum für Astronomie, Universität Heidelberg, Mönchhofstr. 12-14 69120, Heidelberg, Germany; iberent@ari.uni-heidelberg.de

<sup>3</sup> JILA, University of Colorado, Boulder, CO 80309-0440, USA; shlosman@pa.uky.edu

<sup>4</sup> Department of Physics and Astronomy, University of Kentucky, Lexington, KY 40506-0055, USA

(Debattista & Sellwood 1998, 2000). However, at higher resolution, even collisionless numerical bars seem to grow in length towards their CR radius by capturing disk orbits and so remain “fast” (Martinez-Valpuesta et al. 2006). Furthermore, the addition of gas may stabilize the bar against braking and results in its speedup instead for prolonged time periods (Romano-Diaz et al. 2008).

Some studies claim that bars may destroy the cuspy profiles of DM halos predicted by the CDM cosmology (e.g., Dubinski & Carlberg 1991; Navarro et al. 1996), thus alleviating an apparent contradiction between the inferred density profiles of DM halos from galactic rotation curves and this theoretical expectation in some cases (Weinberg & Katz 2002; Holley-Bockelmann et al. 2005; Weinberg & Katz 2007b). Simulations demonstrating cusp destruction use rigid, ellipsoidal bars — their applicability to self-consistent dynamical systems is suspect. Also, there has been some concern about artificial  $m = 1$  instabilities arising from using a fixed center in  $N$ -body field expansion methods (Sellwood 2003; McMillan & Dehnen 2005). Current studies have obtained contradictory results on the efficiency of angular momentum transport to the cusp. Weinberg & Katz (2007a) have emphasized the importance of numerical resolution and, specifically, of the total particle number in simulations. Since the transport of angular momentum operates mainly through low order resonances between the bar pattern speed and halo orbital frequencies, only a small fraction of the halo mass participates. Without adequate particle numbers then, they argue that torques associated with resonant populations may be under-sampled, leading to a spurious calculation of angular momentum transport and, therefore, the evolution of the bar overall. Weinberg & Katz (2007b) estimate that at least  $10^8$  particles and maybe more may be necessary to sample the phase-space densely enough to converge to the correct answer. Recently, Sellwood (2008) has disputed this claim in simulations with rigid bars in spherical, isotropic halos with  $\sim 10^8$  particles arguing that the resonances are broader than they claim.

In this paper, we address the issue of the numerical convergence of bar evolution using a series of  $N$ -body simulations of the bar instability in a self-consistent model galaxy. We analyze bar growth in a bar-unstable  $N$ -body disk. In contrast to other work, we employ new galactic models based on the methods of Widrow & Dubinski (2005), and carry out simulations with substantially greater numerical resolution than reported in the literature. The galaxy is described by a well-defined distribution function for an exponential disk embedded within a DM halo with an  $r^{-1}$  density cusp, based on a truncated Navarro, Frenk & White (1996, NFW) profile. These models are formally in dynamical equilibrium but are bar-unstable. Since they are defined by a distribution function, their  $N$ -body realizations are equivalent, independent of the particle numbers. Hence, this study can probe the effect of numerical resolution on collisionless galaxy evolution. Our goal is to quantify the behavior of a number of specific parameters describing the bar instability as a function of particle number, including the bar strength amplitude,  $A_2$ , as given by the  $m = 2$  Fourier mode, as well as its pattern speed evolution, angular momentum transport, and evolution of the DM density profiles, particularly in the

region within the halo characteristic NFW scale radius,  $r_s$ . We also perform an orbital spectral analysis of halo and disk particles, to quantify the effect of the low order resonances responsible for angular momentum transport (Athanasoula 2002; Martinez-Valpuesta et al. 2006).

The plan of the paper is as follows. In §2, we provide a description of the galactic models and the  $N$ -body experiments to study the bar instability. In §3, we present results on the bar growth and the evolution of pattern speed as a function of numerical resolution. In §4, we examine the evolution the DM halo density profile as a function of numerical resolution. In §5, we study the low order resonances between the bar and the halo particles using orbital integrations and spectral analysis and again compare results at different resolutions. We also examine the details of the evolution of the halo phase space density in our highest resolution models. We conclude with a discussion of the importance of numerical resolution in these experiments and comment on the reliability of current work in studies of disk galaxy formation and dynamics.

## 2. METHODS

### 2.1. Initial conditions: An exponential disk with a cuspy dark halo

The main goal of this study is to characterize the bar instability in terms of mass resolution. The galaxy models of Widrow & Dubinski (2005) (WD models herein) are ideal for this purpose since they are derived from a composite 3-integral distribution function (DF)  $f \equiv f_{\text{disk}}(E, L_z, E_z) + f_{\text{halo}}(E)$ . The disk model has an exponential radial profile and  $\text{sech}^2 z$  vertical profile. The disk DF  $f_{\text{disk}}$  is a 3D extension of the 2D function introduced by Shu (1969) using the vertical energy  $E_z = 1/2 \dot{z}^2 + \Phi(R, z) - \Phi(R, z = 0)$  as an approximate third integral (Kuijken & Dubinski 1995). This DF applies in the epicyclic approximation with  $\sigma_{R,\phi,z} \ll v_c$  and so the vertical energy is approximately constant. This leads to triaxial velocity ellipsoids in the disk models as seen in real spiral galaxies. These models generally provide near equilibrium initial conditions and show negligible transient behavior at startup (Widrow & Dubinski 2005). The halo DF  $f_{\text{halo}}$  describes a truncated spherical, isotropic NFW model. When the two DFs are combined, the net halo density profile changes slightly from the NFW form and is flattened along the  $z$ -axis near the center, but preserves the  $r^{-1}$  central cusp. A suitable choice of parameters allows the construction of a realistic model of bulgeless spiral galaxy with a cosmologically inspired DM halo. Since the models are derived from a distribution function, particle distributions for  $N$ -body experiments can be generated by direct Monte-Carlo sampling.

For the experiments described below, we initially generate a model containing 18M disk particles and 100M halo particles with both disk and halo particles having approximately the same mass. The halo is non-rotating. Lower resolution models are generated by subsampling this larger model in factors of ten and hence creating a sequence of models containing numbers of particles in the range  $1.18 \times 10^4$ – $8$ . One further model is generated with a multi-mass DM halo to increase the particle number density in the core by another two orders of magnitude.

The particle mass is weighted as an approximate step function in angular momentum  $m \sim m(L)$  such that low angular momentum particles near the halo center below a characteristic angular momentum  $L_c$  would have a lower mass. The number density at the center of this model is more than  $100\times$  greater so the effective particle number is  $\approx 10^{10}$  for this simulation. We describe the details for generating the multi-mass model below. Our highest resolution simulations have large enough particle numbers to probe the divergence in numerical behavior discussed by (Weinberg & Katz 2007a).

Each model is generated and simulated in units with  $G = 1$  and physical quantities are of order unity. We have designed the model as a proxy for the Milky Way without a bulge, so natural units for this comparison are  $L = 10$  kpc,  $M = 10^{11} M_\odot$ ,  $V = 207.8$  km s $^{-1}$  and  $T = 47.2$  Myr. By design, the model mass profile closely resembles the one examined by Martinez-Valpuesta et al. (2006). Moreover, the central density cusp is better resolved and the initial conditions are in a better equilibrium, since they are sampled from a DF. Throughout this paper we present results in physical units.

The galaxy mass model is presented in Figure 1 as a rotation curve decomposition. We use an exponential disk with radial scale-length 2.85 kpc and an exponential vertical scalelength of 250 pc and a total mass  $5.5 \times 10^{10} M_\odot$ . The disk is truncated smoothly at  $R = 21$  kpc equivalent to 7.4 scale lengths. The NFW halo scale radius in the DF of the WD model is set to  $r_s = 10$  kpc but results in an effective scale radius of  $r_s = 4.3$  kpc as measured by a least-squares fit to the density profile. The peak circular velocity of the DM halo is  $v_{max} = 0.77$  (160 km s $^{-1}$ ). We note that the smaller scalelength is not due to an adiabatic contraction, but is the result of combining two distribution functions (Widrow & Dubinski 2005) — the extra concentration of mass from the potential of the disk causes the halo potential derived from the NFW DF to be more concentrated as well when calculating the self-consistent potential for the model. The halo extends to a truncation radius of  $r = 260$  kpc and has a total mass  $M = 3.0$  units ( $3.0 \times 10^{11} M_\odot$ ). The final model is a realistic facsimile of an exponential disk galaxy with a cuspy DM halo. The square of the radial velocity dispersion  $\sigma_R^2$  of these models follows the same exponential radial decline as the surface density with  $\sigma_R^2 \sim \exp(-R/R_d)$ . We choose a central value  $\sigma_{R,0} = 104$  km s $^{-1}$ , so that the Toomre  $Q$  is  $Q = 1.1$  at  $R = 10$  kpc. The disk is, therefore, relatively cold and responsive. This model is in dynamical equilibrium but also is strongly bar-unstable. Our analysis focuses on the development of the bar instability in simulations of this model with different particle numbers. At this point, we also present the final state of the mass model after 9.4 Gyrs of dynamical evolution for direct comparison to the initial state but defer the discussion until later (Fig. 2).

## 2.2. Multi-mass model

A common way of increasing mass resolution with a number of particles is to use a range of masses, assigning low mass particles to the center where the action is and high mass particles to the periphery (Sigurdsson et al. 1995). We therefore build an additional model that weights the halo particle mass as a monotonically increasing function of orbital angular momentum  $L = |\mathbf{r} \times \mathbf{v}|$ ,

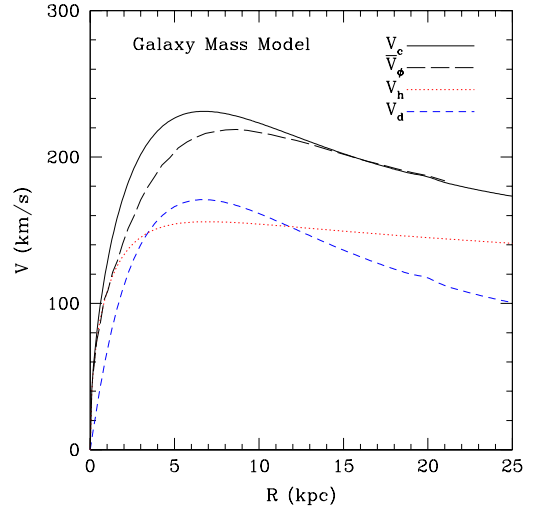


FIG. 1.— Initial circular velocity curve of the mass model showing the contributions from the disk and the DM halo. We also plot the mean tangential velocity in the disk to show the effect of an asymmetric drift on the rotation curve.

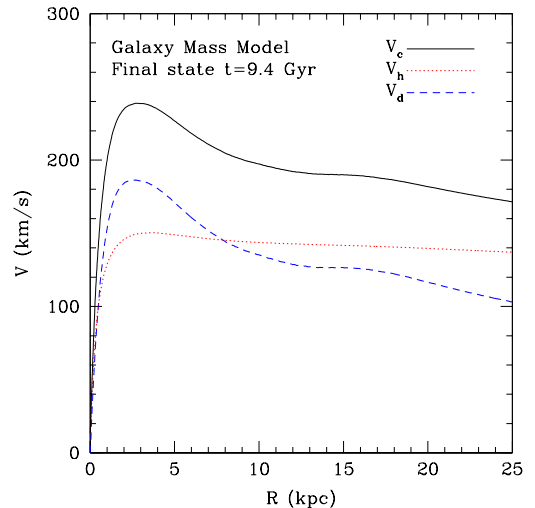


FIG. 2.— Final circular velocity curve of the barred galaxy mass model at  $t = 9.4$  Gyr. We show the contributions from the barred disk and the DM halo. The disk component is estimated by axisymmetrizing the barred disk and calculating  $v_d^2 = R\partial\Phi/\partial R$ .

to increase the number density of particles in the region where the bar forms and where the low order resonances occur. The strategy is to define a mass weighting function  $W(L)$  such that particles with low angular momentum and orbits with small pericenters also have small mass, while those with large angular momentum and pericenters beyond the edge of the disk have a higher mass. The halo DF is normalized by this weighting function, so that the number density of particles derived from Monte Carlo sampling will be larger for smaller values of  $L$ . In this way, the probability of selecting a particle with smaller  $L$  is greater than with larger  $L$ . The biased number density is then corrected to represent the model with the original DF by multiplying the particle mass by

$W(L)$ . The weighting function is normalized so that the mass of a particle in the initial distribution is given by

$$m_i = \frac{M_{\text{halo}} W(L_i)}{\sum_i W(L_i)} \quad (1)$$

The choice of the functional form of  $W(L)$  is arbitrary at some level according to the needs of the problem but in our case it should be monotonically increasing with  $L$ . We use the step-like weighting function in  $L$

$$W(L) = 1.0 + \frac{W_1 - 1}{1 + (L/L_c)^{-\alpha}} \quad (2)$$

where  $L_c$  is a characteristic angular momentum for the step,  $\alpha > 0$  is an exponent and  $W_1$  is the asymptotic value of weighting function for large angular momentum. When  $W$  is plotted versus  $\log L$  it takes the form of a step function where the steepness of the transition at  $\log L_c$  depends on the choice of  $\alpha$ . In practice, we truncate the function at minimum and maximum values of  $L$  at  $L_{\min}$  and  $L_{\max}$  and set the weight to the value at these limits beyond the endpoints.

After some experimentation, our final choices for these parameters are  $W_1 = 10^4$ ,  $L_{\min} = 10^{-3}$ ,  $L_c = 3$ ,  $L_{\max} = 7$ , and  $\alpha = 0.9$ . The choice of  $L_c$  corresponds to particles moving at the circular velocity at a radius of  $R = 4.1$  (41 kpc) about twice the radius of the disk. The choices of  $L_{\min}$  and  $L_{\max}$  limit the dynamic range of masses to about 600 with the least massive particles weighing in at 0.5% the equivalent mass for a single-mass model and the most massive particle weighing in at  $3 \times$  the equivalent mass. For comparison, the single-mass particle in the  $N = 10^8$  halo is  $3 \times 10^3 M_\odot$ , while in the multi-mass model, the particle masses range from  $16 M_\odot$  for small  $L$  to  $10^4 M_\odot$  for the most massive particles in outskirts of the halo.

We plot the ratio of the particle number density in the multi-mass model to the equal mass particle number density in Figure 3. The number density is about  $200 \times$  greater within the central 100 pc of the model and about  $10 \times$  at  $R = 1$  kpc.

### 2.3. Simulations

We simulate these models using a parallelized treecode Dubinski (1996) for 200 time units (9.4 Gyr), permitting us to see the development of the bar instability through various phases roughly over a Hubble time. We soften gravity with a Plummer model kernel and vary the softening length  $\epsilon$  according to the particle numbers of the simulation roughly in proportion to  $N^{-1/3}$ . The median force errors are 0.1% for the chosen treecode parameters. Simulation parameters are given in Table 1.

A constant timestep is used for all of the simulations (see Table 1). The circular orbital period in the mass model at the smallest softening radius of  $\epsilon = 10$  pc is about 15 Myr and so is resolved by 30 timesteps. Plummer softening smooths gravity over a few softening lengths so the smallest resolved radius of these simulations is  $\approx 3\epsilon$ . We find that total binding energy is typically conserved to within 0.2% and angular momentum is conserved to within 1% over the course of the runs. Each simulation, with the exception of the multi-mass case, is repeated twice with a different random realization to explore statistical variance in the growth of the bar mode.

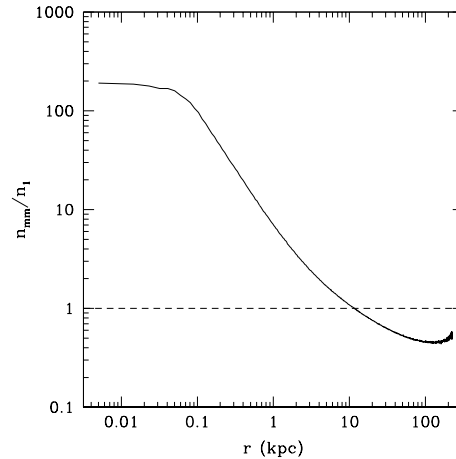


FIG. 3.— The ratio of the number density of the multi-mass 100M particle halo to the single-mass 100M halo. The distribution function is sampled such that particle mass is weighted by a smoothed step function of total angular momentum. Particles with low angular momentum have small mass and those with high angular momentum have low mass (see text). The particle density is more than 100 times higher within 0.1 kpc and at least 10 times higher within 1 kpc. For  $R > 10$  kpc the number density drops gradually to about half the single-mass case. The effective numerical resolution at the center of simulation is therefore  $N_h \sim 10^{9-10}$ .

TABLE 1  
SIMULATION PARAMETERS

Model	$N_h$	$N_d$	$\epsilon$ (pc)	$\delta t$ (kyr)	$N_{\text{steps}}$
m10K	$10^4$	$1.8 \times 10^3$	200	470	20000
m100K	$10^5$	$1.8 \times 10^4$	100	470	20000
m1M	$10^6$	$1.8 \times 10^5$	50	470	20000
m10M	$10^7$	$1.8 \times 10^6$	20	470	20000
m100M	$10^8$	$1.8 \times 10^7$	10	470	20000
mm100M	$10^8$	$1.8 \times 10^7$	10	235	40000

NOTE. — The model mm100M is the multi-mass model.

Figure 4 shows an animation<sup>5</sup> of the evolution of the disks in six models in face-on and edge-on views. The lowest resolution model m10K demonstrates how insufficient particle numbers can lead to spurious results. A bar develops immediately in the 1.8K particle disk but devolves into a compact rapidly tumbling object. In retrospect, early galaxy formation simulations that introduced the angular momentum problem (e.g., Navarro & Steinmetz 2000) only contained 2K particles, so part of the problem may have arisen from exceedingly noisy evolution of a bar mode. The m100K model with an 18K particle disk still appears noisy, though the buckling instability is clearly visible. The disk is visibly thicker than the higher resolution models, however, and the bar is not as pronounced. Disk heating by bombardment of halo particles is a problem. The time of onset of the bar instability is delayed as  $N$  increases, reflecting the effect of Poisson noise. Since the bar instability grows exponentially from density fluctuations in the ini-

<sup>5</sup> Quicktime animations are available at the website [www.cita.utoronto.ca/~dubinski/BarsInCuspyHalos/](http://www.cita.utoronto.ca/~dubinski/BarsInCuspyHalos/)

tial conditions, larger  $N$  simulations will have smaller initial amplitudes and, therefore, longer times to saturate.

Figure 5 displays the evolution of the multi-mass halo model with the 18M particle disk close-up and two perpendicular edge-on views simultaneously. Figure 6 refers to the face-on view in a frame co-rotating with the bar to emphasize the growth of the bar mode. This model starts very quietly and there is little visible structure until  $t \approx 1$  Gyr when the bar begins to emerge. The bar grows from the inside out, gradually increasing in length until it reaches a maximum length at nearly the CR radius around  $t = 2$  Gyr. At this time, the bar also excites a prominent, bi-symmetric spiral structure. After saturation, the bar re-structures itself, becoming more centrally concentrated and weakening, as it settles into a quasi-steady state. After settling, the pattern speed begins to decline and the bar's length increases slowly, since the CR radius is increasing and the bar can capture additional orbits in the disk. The other notable event is the vertical buckling instability that occurs around  $t = 3.5$  Gyr creating a characteristic X-shaped structure as various families of orbits establish themselves causing the bar to thicken vertically. By the end of the simulation, the inner bar transforms into a peanut-shaped bulge though it still is obviously elliptical in the face-on view.

Figure 2 shows the rotation curve decomposition for the model at the final time  $t = 9.4$  Gyr. We rotate particles in the final barred disks to random angles  $\phi$  to make the disk potential axisymmetric and then compute the disk rotation curve component through  $v_d^2 = R\partial\Phi/\partial R$ . The halo rotation curve component is estimated from the spherically-averaged density profile of the dark matter. The collapse of the bar leads to a concentrated bulge-like component and the rotation curve flattens slightly creating a galaxy model that more closely resembles real systems. The halo profile at large radii does not change a lot but we will see in further analysis discussed below that there is slight increase in the central density. In this barred galaxy model, both the stars and dark matter have comparable contributions to the rotation curve in the inner regions.

In the next section, we quantify these various effects and look for differences in resolution with the hope of finding numerical convergence in physical behavior.

### 3. BAR GROWTH AND PATTERN SPEED EVOLUTION

The growth of the bar instability is measured by the bar strength with the  $m = 2$  Fourier amplitude of the surface density,  $A_2$ , given by:

$$A_2 = \frac{1}{M} \sum_{j=1}^N m_j \exp(2i\phi_j); R < R_c \quad (3)$$

where the summation is performed over a list of particles with masses  $m_i$  at angle  $\phi_i$  in the  $x-y$  plane within some cut-off radius  $R_c$ . The normalized amplitude  $|A_2|$  versus time measures the growth rate of the bar instability and the phase angle  $\phi = 0.5 \tan^{-1}[\text{Im}(A_2)/\text{Re}(A_2)]$  with time permits measurement of the pattern speed by numerical differentiation.

All models were simulated for 200 time units (9.4 Gyr) and every 10 (or 20 in the multi-mass case) timesteps a face-on surface density image was generated from the

particle distribution resulting in a sequence of 2000 images. These image sequences were analyzed to determine  $A_2$  by summing over pixels rather than particles in equation 3. The amplitudes and phase angles were then tabulated as a function of time to determine the rate of growth of the bar and the pattern speed evolution. Pattern speed is estimated by simply differencing angles in subsequent pairs of phase angles and dividing by the time interval. In practice, we only use values every 50th snapshot to smooth out the noise in these parameters introduced by limited numbers of particles. We show below that higher resolution simulations produce smoother curves of bar growth and pattern speed evolution.

#### 3.1. Numerical Accuracy

We first discuss the behavior of the bar instability as a function of integration timestep. Klypin et al. (2008) have claimed that very small timesteps are necessary to resolve the dynamics of bars because of the possible development of cuspy density profiles in the forming bulge-bar system. Our simulations use a single timestep chosen to resolve the smallest dynamical timescale in the model. Multiple timestepping schemes often use the criterion,  $\delta t = (2.8\epsilon/|\mathbf{g}|)^{1/2}\eta$  where  $\epsilon$  is the Plummer softening or equivalent,  $|\mathbf{g}|$  is the acceleration and  $\eta$  is a free parameter usually chosen with a recommended value of  $\eta = 0.2$  (e.g., Springel et al. 2001). For density laws following  $\rho \sim r^{-1}$  the central acceleration is constant. The highest value of the acceleration in our galaxy model occurs in the center, and using it with  $\eta = 0.2$  we arrive at  $\delta t = 0.01$  (470 kyr) for  $\epsilon = 50$  pc and  $\delta t = 0.004$  (190 kyr) for  $\epsilon = 10$  pc. Plummer softening of course reduces the maximum value near the center and it formally falls to zero at  $r = 0$ . We see below that there is only a modest increase in the central density evolution, so the maximum value of  $|\mathbf{g}|$  does not change by much over the course of the run.

The smallest orbital period is  $\sim 15$  Myr for an orbit with  $R \sim \epsilon$  and our chosen timestep is  $\delta t = 470$  kyr, so these orbits are resolved with approximately 30 timesteps. For our highest resolution simulation, we use  $\delta t = 235$  kyr to account for the smaller softening radius. The fraction of particles with orbital periods less than 20 Myr is approximately 0.1% based on an analysis of the radial frequency of 100K testparticle orbits sampled from the halo integrated within the rigid potential of our mass model. If the timestep is too large, orbits near the center will be unstable and create an artificial constant density core. Another possible problem occurs for highly radial orbits with longer periods that pass close to the central cusp. Our orbital analysis showed that approximately 0.13% of orbits change binding energy by more than 1% over a 9.4 Gyr integration with  $\delta t = 470$  kyr. All of these orbits had small pericentric radii  $\sim 100$  pc. We therefore expect a small fraction of highly radial orbits to diffuse artificially through energy space. We demonstrate here that the single timesteps of  $\delta t = 235$  and 470 kyr are sufficiently small to resolve the dynamics for our choices of the Plummer softening radius.

To test for numerical convergence, we have re-run the model m1M using *single* timesteps over the range of  $\delta t = 15 - 940$  kyr for a time of 4.7 Gyr. The model with  $\delta t = 15$  kyr required 320K single steps. This galaxy model has  $N_d = 180\text{K}$  and  $N_h = 1\text{M}$  and a Plummer

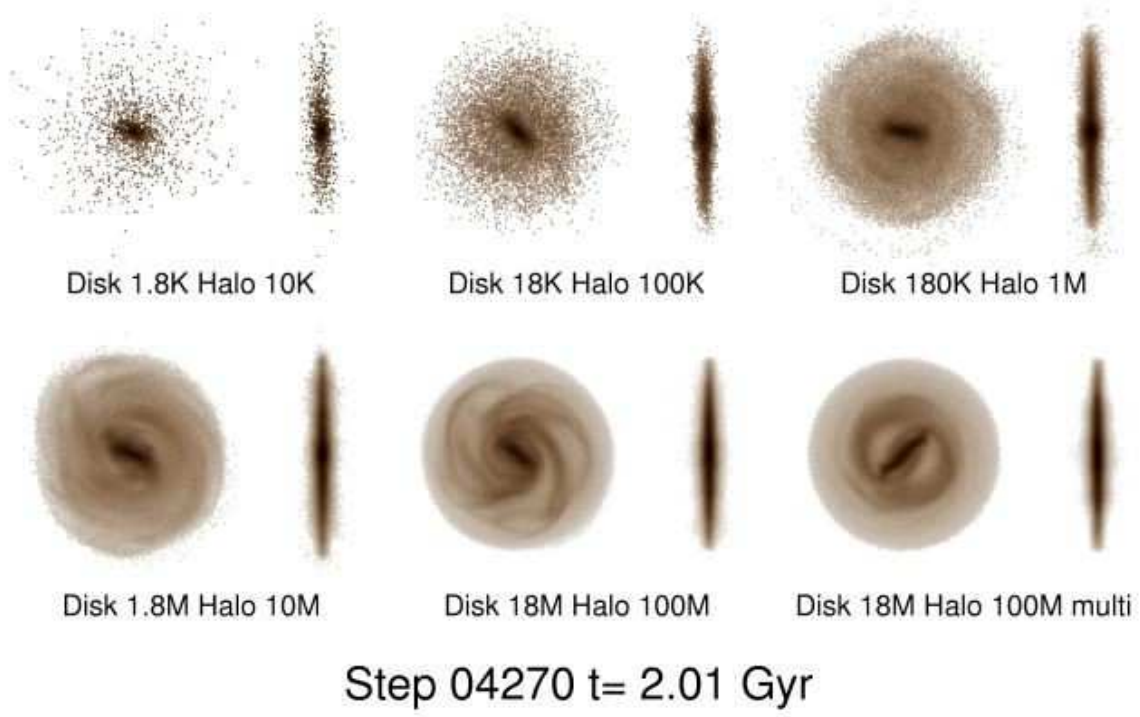


FIG. 4.— A comparison of the evolution of the bar instability in 6 simulations with increasing particle number  $N$ . The formation of a bar is delayed for simulations with larger  $N$  since the Poisson seed noise has a lower amplitude and it takes longer for the instability to grow in the linear regime. The lowest resolution simulations suffer from heating while the general behavior converges at higher resolution for  $N \geq 10^6$  (see Video 1)



FIG. 5.— Evolution of the multi-mass model in the inertial frame showing the face-on view and two perpendicular edge-on views. The bar grows from the inside out first evolving into a thin bar extending to the co-rotation radius and then settling down into a less elongated ellipsoid. The buckling instability vertically thickens the bar into a peanut-shaped bulge at later times. The bar grows in length as angular momentum is lost to the halo and new orbits are captured with the co-rotation radius (see Video 2).

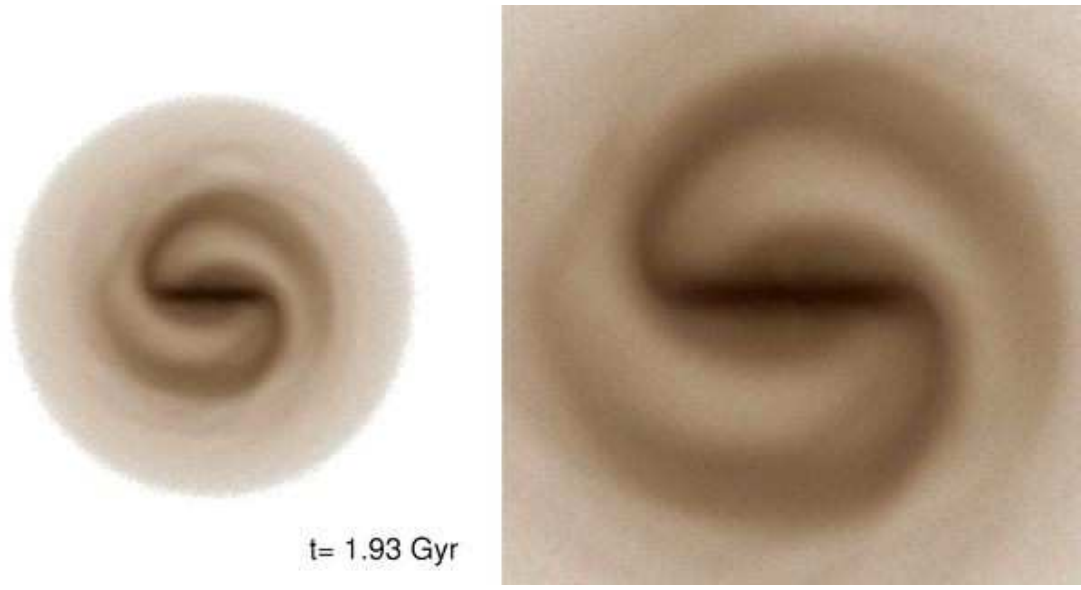


FIG. 6.— Evolution of the multi-mass model in the co-rotating frame showing a global and close-up of the face-on orientation. The co-rotation radius is clearly visible at the distance where particles reverse the direction of circulation around the bar. The bar evolves to extend to the co-rotation radius and remains “fast” (see Video 3).



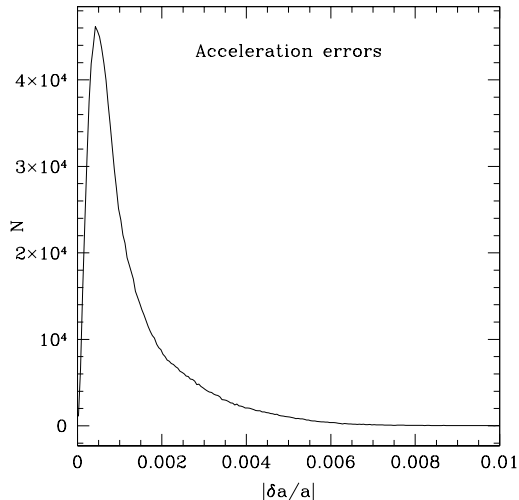


FIG. 7.— Relative acceleration errors for the parallel treecode for runs with  $N = 1.18\text{M}$  particles. Errors are estimated by comparing accelerations computed with our preferred treecode opening angle parameter  $\theta = 0.9$  with quadrupole order corrections to the exact values determined from a direct calculation. The mean relative error is 0.13% with a median value of 0.085%. Note the opening angle criterion for the parallel treecode is more conservative than standard definitions and so a larger value of  $\theta$  still results in relatively small acceleration errors (Dubinski 1996).

softening length of  $\epsilon = 50$  pc. We examine different metrics of the system evolution including bar growth, pattern speed evolution and the final density profile of both the stars and DM all as a function of timestep.

### 3.1.1. Acceleration Errors

We first comment on the accuracy of the accelerations determined using the parallel treecode (Dubinski 1996). Normally force accuracy is not discussed despite a large variety of algorithms used to compute gravitational forces. We present our errors here so that other researchers may compare to their own standards of numerical accuracy. Figure 7 shows the distribution of relative acceleration errors for our preferred treecode parameters. We use an opening angle tolerance  $\theta = 0.9$  with quadrupole corrections using a more conservative cell opening criterion than normally described that gives more accurate acceleration values for a given  $\theta$  than standard definitions (Dubinski 1996). Errors are determined by comparing accelerations from the treecode method to a direct force calculation. The median and mean relative acceleration errors are 0.085% and 0.13% respectively with 99.7% ( $3\sigma$  limit) of acceleration errors less than 0.7%.

### 3.1.2. Energy Conservation

The evolution of the error in total binding energy of an  $N$ -body system is a useful indicator of the fidelity of the results and can reveal potential problems with the integration scheme or choice of timestep. Figure 8 shows the change in total binding energy as function of timestep. The largest timestep of  $\delta t = 940$  kyr shows a strong systematic drift in energy reflecting the inadequate timestep resolution for a significant fraction of orbits. There is a smaller drift in the energy with a relatively small error

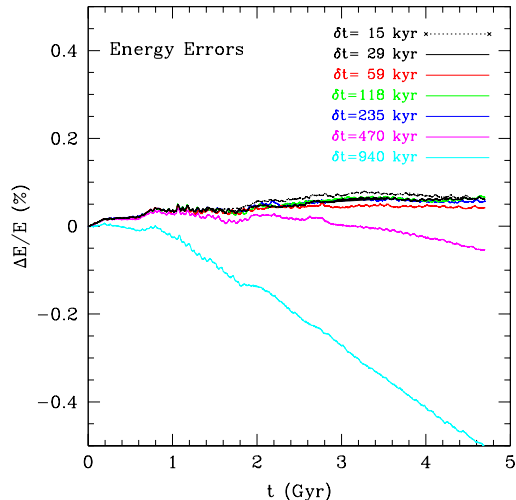


FIG. 8.— Total energy errors for runs with different time-steps  $\delta t$ . The simulation with  $\delta t = 940$  kyr shows a systematic drift due to inadequate numbers of timesteps to follow orbits within the core. There is a lesser drift for the timestep  $\delta t = 470$  kyr but the error has only grown to 0.1% by the end of the run. All timesteps with  $\delta t < 470$  kyr show very little drift.

of 0.1% over 4.7 Gyr with our main choice of  $\delta t = 470$  kyr and clear convergence with no systematic effects with  $\delta t \leq 235$  kyr. We, therefore, conclude that  $\delta t = 470$  kyr is adequate for our models. We show below that there are no substantial differences between various metrics of the properties of the bar and halo when using timesteps with  $\delta \leq 470$  kyr.

### 3.1.3. Bar Evolution versus Timestep

We measured both bar growth and pattern speed evolution as a function of timestep in the m1M model with  $N_d = 180\text{K}$  and  $N_h = 1\text{M}$ . Figure 9 presents the evolution of the bar growth parameter  $|A_2|$  measured within  $R < 5$  kpc versus timestep. During the linear growth phase of the bar instability, all simulations track one another very closely. However, after the bar instability saturates around  $t \sim 1$  Gyr the behavior is quite variable and erratic for different choices of the timestep. The time of bar buckling shown by the sudden secondary drop in  $|A_2|$  changes with different timesteps and lies in the range  $t = 1.8 - 2.5$  Gyr. There is no monotonic trend with timestep. The range of variability is the same as our study of independent random realizations in § 3.2. The root cause of this behavior is probably the dynamical chaos inherent to this late evolution of the bar instability. The detailed  $N$ -body solutions for individual particles diverge exponentially for different choices of integration step in the nonlinear regime of dynamical evolution. Despite this divergence on the individual particle level, the global properties of the resulting bar are similar as we shall see.

An analysis of the pattern speed evolution shows consistent results for all timesteps (Fig. 10). The agreement in the linear regime evolution until the bar instability saturates at  $t \sim 1$  Gyr is very close, after which the detailed evolution show differences. There is a  $2 - 4 \text{ km s}^{-1} \text{ kpc}^{-1}$  scatter in the pattern speed at any given time but the general declining trend is the



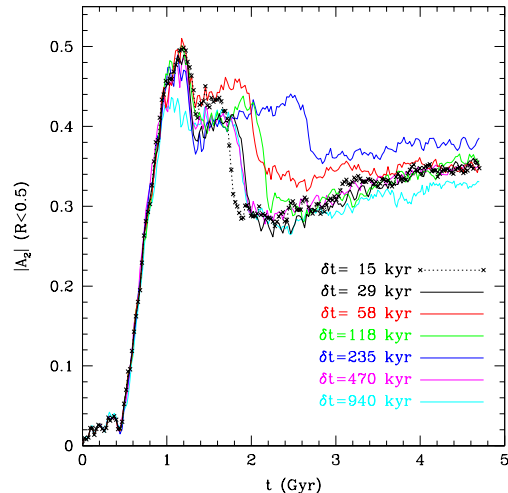


FIG. 9.— Evolution of the Fourier component,  $A_2$  for stars with  $R < 5$  kpc for a single model with  $N_d = 180K$  and  $N_h = 1M$  particles with global timesteps spanning the range of  $\delta t = 15$  kyr to 940 kyr. The linear growth phase of the bar is almost identical until the bar instability saturates at  $t \sim 1$  Gyr. The subsequent nonlinear evolution shows a wide range of behavior for different timesteps with no monotonic trend. The nonlinear phase of the bar instability involves chaotic orbits and so the slight variations introduced by the round-off error of different discrete timesteps lead to divergent evolutionary behavior. The main manifestation of this chaos are different times for the onset of the buckling instability ranging from 1.8-2.5 Gyr having no dependence on the chosen timestep. Nevertheless, the behavior is qualitatively similar after the buckling instability with a steady rise of  $|A_2|$  at late times as the bar lengthens.

same over the course of the run. The observed scatter is consistent with the same scatter seen in different random realizations (Fig. 13). The mean and variance of the pattern speed at  $t = 4.7$  Gyr for all timestep runs is  $\Omega_b = 16.6 \pm 0.7 \text{ km s}^{-1} \text{ kpc}^{-1}$ . We conclude that our choice of timestep leads to a consistent evolution of the bar pattern speed.

#### 3.1.4. Stellar and Halo Central Density versus Timestep

As a final metric of the accuracy of the simulations versus timestep, we measured the spherically averaged density profile of the stars and DM at the last snapshot at  $t = 4.7$  Gyr. At this time, the bar has buckled and has formed a concentrated bulge-like object within the halo that has become more dense itself in response to this new bulge (see below). Figure 11 shows the stellar density profile within  $r < 1$  kpc of the center for runs with different timesteps. The density profiles for the bar/bulge are consistent within the error bars for  $\delta t \leq 470$  kyr. There is some random scatter in the inner radial bins since there are only a few hundred particles at these small radii. The model with  $\delta t = 940$  kyr forms a core with constant density within  $r < 200$  pc though the density is only 0.3 dex (about  $2\times$ ) smaller than the density in the first radial bin of the smaller timestep runs. The runs with  $\delta t \leq 470$  kyr agree within  $\pm 0.1$  dex for  $r < 200$  pc and much of that error is due to small particle numbers with  $\sim 10^2$  particles per bin.

We also measured the spherically-averaged density profile of the DM at  $t = 4.7$  Gyr (Fig 12). We have approximately  $6\times$  as many particles per bin and so the random

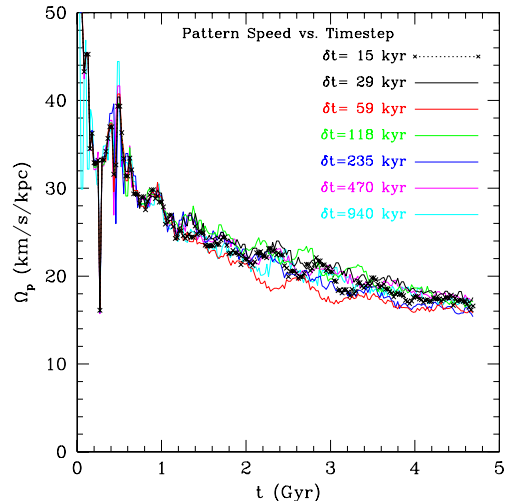


FIG. 10.— Evolution of the pattern speed  $\Omega_b$  for models with  $N_d = 180K$  and  $N_h = 1M$  and timesteps spanning the range of  $\delta t = 15$  kyr to 940 kyr. During the linear growth phase of the bar until  $t \approx 1$  Gyr, the pattern speed evolution is almost the same. Once the bar becomes nonlinear, there is a small scatter in the detailed behavior of the pattern speed with a variation of  $2 - 4 \text{ km s}^{-1} \text{ kpc}^{-1}$  at any given time. By the end of the runs, the results converge with the mean and variance of the pattern speed  $\Omega_b = 16.6 \pm 0.7 \text{ km s}^{-1} \text{ kpc}^{-1}$  at  $t = 4.7$  Gyr. There is no strong dependence of the pattern speed evolution on the choice of timestep.

errors are smaller. The DM density profiles are consistent for  $\delta t \leq 470$  kyr suggesting we have adequate time resolution for the halo density evolution. Again, we see the development of an artificial constant density core in the simulation with  $\delta t = 940$  kyr. This timestep is clearly too large and does not adequately follow short period orbits in the core. However, simulations with timesteps smaller than  $\delta t \leq 470$  kyr adequately follow the dynamics of the evolution of the DM halo.

In summary, we have presented the force accuracy and total energy evolution of our simulations with different timesteps. We have also shown that our results converge experimentally for  $\delta t \leq 470$  kyr according to different metrics of the bar evolution including pattern speed evolution and stellar and dark matter density central density profile. We note that there is a random behavior for the time of onset of the buckling instability for different choices of timestep which probably results from the chaotic nature of this dynamical system. (This was shown explicitly by Martinez-Valpuesta & Shlosman 2004.) If the timestep is too large, the main effect is to create an artificial constant density core. Particles with short orbital periods are numerically unstable and are scattered out of the center creating the core. In the subsequent analysis, we show that the central density continues to increase at smaller radii with higher mass resolution. If our timestep was too large, one might expect instead to see the onset of a artificial constant density core of a fixed radius set by the timestep and independent of the mass resolution. We do not observe this behavior. We also do not see a sudden change in behavior of the pattern speed evolution at a critical timestep as seen by Klypin et al. (2008). We, therefore, conclude that we have adequate time resolution to follow the dy-

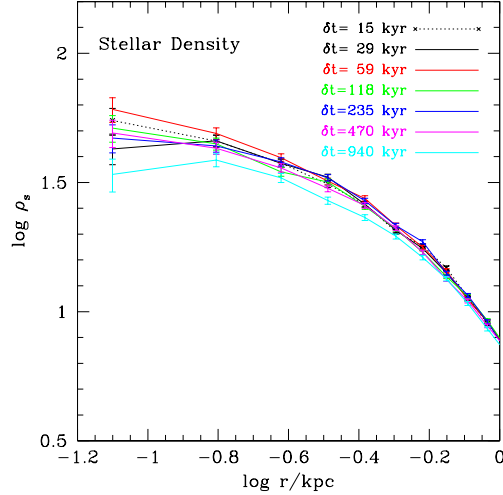


FIG. 11.— The spherically averaged density profile of the stellar component that includes the buckled bar and disk at  $t = 4.7$  Gyr for runs with different time-steps. The error bars are  $1-\sigma$  estimates of the  $\sqrt{N}$  Poisson error in the density due to discrete sampling e.g., the inner most bins contain  $\sim 100$  particles so the  $1-\sigma$  error in density is about 10%. For time-steps with  $\delta t \leq 470$  kyr, the density profiles are consistent within the random errors. The run with  $\delta t = 940$  kyr shows the formation of an artificial core due to an insufficient number of time steps to follow orbits within  $r \sim 100$  pc.

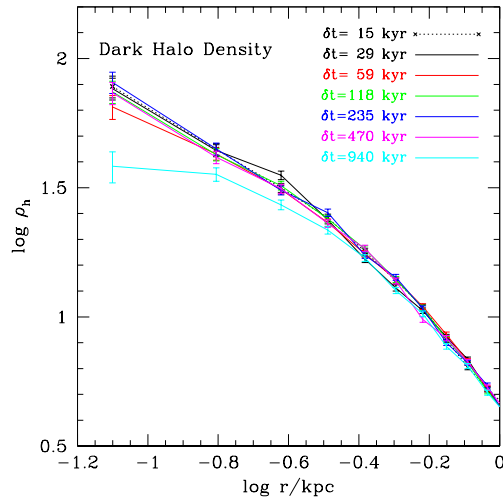


FIG. 12.— The spherically averaged density profile of the dark matter halo at  $t = 4.7$  Gyr for runs with different time steps. The error bars are  $1-\sigma$  estimates of the  $\sqrt{N}$  Poisson error in the density due to discrete sampling. For time-steps with  $\delta t \leq 470$  kyr, the density profiles are consistent within the random errors. The run with  $\delta t = 940$  kyr shows the formation of an artificial core due to an insufficient number of time steps to follow orbits within  $r \sim 100$  pc.

namical evolution of this system all the way down to the radius where Plummer softening dominates.

### 3.2. Models at fixed resolution

Before presenting results on the bar and pattern speed evolution versus mass resolution, it is instructive to un-

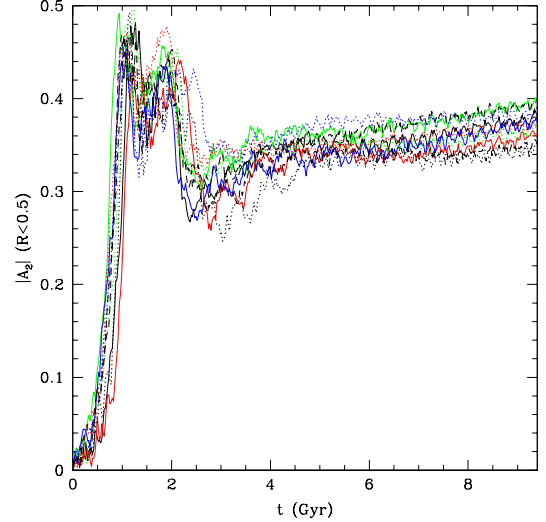


FIG. 13.— Evolution of the Fourier component,  $A_2$  for stars with  $R < 0.5$  for 10 models with  $N_d = 180K$  and  $N_h = 1M$  generated with different initial random seeds. There is a large variation in evolution of  $A_2$  during the formation of the bar over the time interval  $t = 20 - 70$  reflecting detailed differences in the Poisson noise in different random realizations. The plot reveals the approximate scatter in evolutionary behavior expected for different runs.

derstand the variance expected for runs at a fixed resolution. The seed of both spiral and bar instabilities in  $N$ -body simulations is the Poisson noise in the discrete particle distribution of the disk and halo. We, therefore, expect some variation in the detailed behavior of the growth of the bar instability in different random realizations and we quantify it here.

We build ten galaxy models with 1M halos particles and 180K disk particles independently from different Monte-Carlo samplings of the galaxy model DF by using a different initial seed for the random number generator. We measure  $|A_2|$  within a radius  $R < 0.5$  units (5 kpc) which is within the eventual co-rotation radius of the bar. Figure 13 shows the evolution of the bar strength for the 10 runs. The detailed behavior varies significantly for the different runs with the minimum and maximum values of  $|A_2|$  that varying by  $\pm 0.05$  during the bar growth phase between  $t = 1 - 3.3$  Gyr and final values ranging from 0.35-0.40 at  $t = 9.4$  Gyr. While the runs differ in detail there is still a generic behavior with the bar growth saturating around at  $|A_2| \approx 0.5$  and then going through an oscillation before settling down to a value near  $|A_2| \approx 0.3$  around  $t = 3.3$  Gyr. The bar then grows slowly increasing in length as the pattern speed declines.

Fig. 14 shows the pattern speed  $\Omega_b$  evolution for the same 10 runs at fixed resolution. The behavior is similar with the bar starting out with  $\Omega_b \approx 35 \text{ km s}^{-1} \text{ kpc}^{-1}$  declining to a value between  $12 - 14 \text{ km s}^{-1} \text{ kpc}^{-1}$ . The pattern speed evolution is consistent at the 10% level despite the different histories of the bar growth as quantified by  $|A_2|$ .

We, therefore, expect the minimum and maximum values of  $|A_2|$  to vary by about 0.05 units between models and pattern speeds to vary conservatively by  $\pm 2 \text{ km s}^{-1} \text{ kpc}^{-1}$  for stochastic reasons alone.

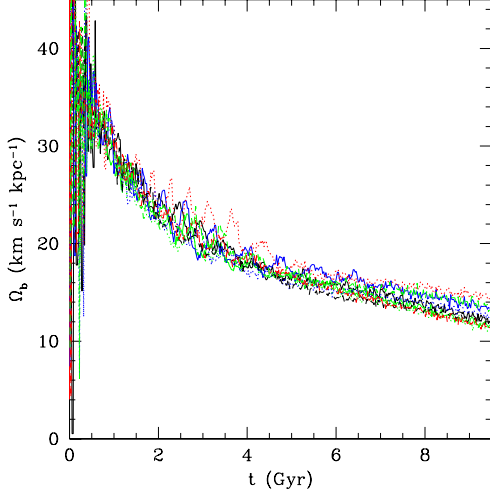


FIG. 14.— Evolution of the pattern speed,  $\Omega_b$ , for 10 models with  $N_d = 180K$  and  $N_h = 1M$  generated with different initial random seeds. The pattern speed is measured by creating a time series of the phase angle of the  $A_2$  component for stars with  $R < 0.5$ . The pattern speed decays after the bar forms as angular momentum is transferred to the dark halo through dynamical friction. While the decay rate is similar, again there is scatter due to statistical variation of the Poisson noise in the initial conditions.

### 3.3. Models with increasing mass resolution

After quantifying the effects of temporal resolution and stochasticity in models at fixed resolution, we go on to examine models of increasing mass resolution with halos containing from  $10^5$  to  $10^8$  particles and the multi-mass model with an effective resolution of  $10^{10}$  particles. Our goal here is to measure carefully bar growth and pattern speed and to single out any differences that are inconsistent with the expected statistical variance. We have simulated 2 models at each resolution in Table 1 with the exception of the multi-mass case where we did only one model.

Figure 15 shows the bar growth for all resolutions plotted as  $\ln |A_2|$  versus time to emphasize the growth of the instability through the linear regime. Spiral and bar instabilities grow from seed density fluctuations in Poisson noise through the swing amplification mechanism (Toomre 1981). In the linear regime, the fluctuations grow exponentially and so  $\ln |A_2|$  is roughly linear in time. The dashed line to the right is parallel to the model growth rates and corresponds to exponential growth with a timescale of  $\tau = 370$  Myr.

Once the perturbation goes non-linear,  $|A_2|$  reaches a maximum value and then oscillates until reaching a steady state as the bar settles into a quasi-equilibrium. All models show a gradual linear rise of  $\ln |A_2|$  after reaching equilibrium but are noticeably offset in the saturation time when going to higher resolution. Since the seed perturbations arise from Poisson noise, the amplitude of perturbations  $\delta$  varies as  $N^{-1/2}$ , so the ratio of amplitudes in two different simulations is  $\delta_1/\delta_0 = (N_1/N_0)^{-1/2}$ . In the linear regime,  $\delta \sim \exp(t/\tau)$ , so the time delay between growing perturbations to reach the same amplitude is  $\delta t \approx \tau \ln(N_1/N_0)^{1/2}$ . Simulations with a factor of 10 more particles will, therefore, be delayed in saturating by a time interval given by

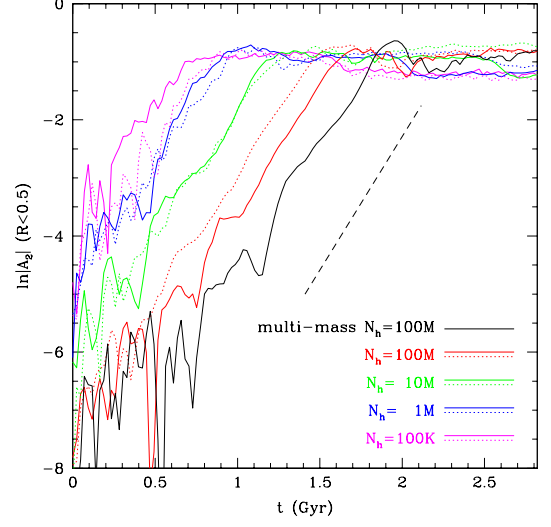


FIG. 15.— Initial growth of the bar strength  $|A_2|$  for stars with  $R < 0.5$  for two model sequences using  $N_d = 18K, 180K, 1.8M, 18M$  with  $N_h = 100K, 1M, 10M, 100M$  respectively. The  $\ln |A_2|$  grows approximately linearly with time independent of the choice of  $N_d$  and  $N_h$  showing the exponential growth of the bar mode. The dashed line shows an exponential timescale that is approximately  $\tau = 370$  Myr. Since the bar grows from the Poisson noise within the disk then we expect the noise amplitude to be proportional to  $N^{-1/2}$ . Based on exponential growth of the bar mode, we expect the time to saturation of  $|A_2|$  to be delayed by roughly  $\delta t \approx \tau \ln(N_1/N_0)^{1/2}$ , e.g., a factor of 10 change in particle numbers leads to a delay  $\delta t \approx 9$ . The difference in saturation times of  $|A_2|$  between the various simulations are roughly consistent with this estimate though there is some variation.

$\delta t \sim \tau \ln 10^{1/2} \approx 1.1\tau$ . With  $\tau \approx 370$  Myr, we expect a time delay of approximately 400 Myr between simulations differing by a factor of 10 in numbers of particles. If we select the time when  $|A_2|$  reaches a maximum as a reference time when the bar saturates and the linear regime ends, we can estimate the time delay between simulations directly. Using the 1M particle run as a zero point, we find delay times of  $\delta t = 280$  Myr for 10M particle models and  $\delta t = 600 - 700$  Myr for the 100M models and  $\delta t = 950$  Myr for the multi-mass 100M model. The noise characteristics of the multi-mass model are more complicated than the simple ideas discussed here and vary across the model but the onset of the bar instability is nonetheless delayed further because of quieter initial conditions. These values are slightly smaller than expected but are in reasonable agreement with the estimated delays from considerations of the growth of Poisson fluctuations. This analysis emphasizes that *the spiral and bar instabilities that arise in N-body simulations of disks are wholly dependent on the initial Poisson noise. In the future, with simulations using more than 10M disk particles it makes sense to control the properties of the noise both in amplitude and power spectrum as done in cosmological simulations.*

Figure 16 and 17 show the evolution of the bar strength when we account for the time delays and allow a comparison of the early and late time evolution. When synchronized this way, the linear growth phase is readily apparent in the evolution of  $\ln |A_2|$  in Fig. 16. In Fig. 17, the plot of the evolution of  $|A_2|$  reveals the details of the non-linear evolution of the bar. The bar strength saturates

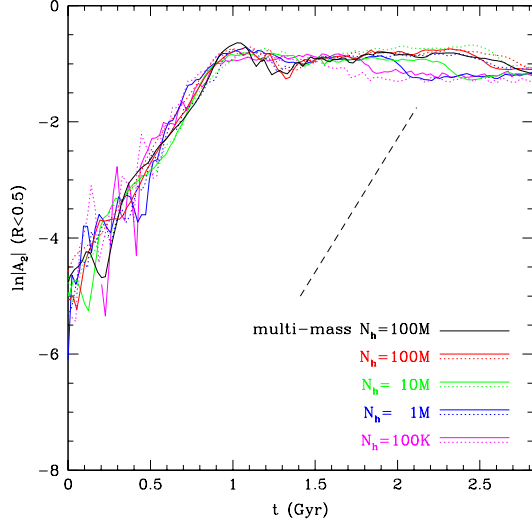


FIG. 16.— Same as Fig. 15 except the curves have been shifted in time so that the linear regime growth phases overlap with the m1M model according to the measured time delays

at a maximum value followed by an oscillation through a minimum and then a slow rise to the end of the simulation. For the most part, the range of behavior between different resolutions is consistent with our expectations of variance from our study of 10 simulations at fixed resolution. However, the highest-resolution multi-mass model dips to a lowest minimum value of  $|A_2|$  and takes more time to grow in the later phase. This difference does lie within the range of stochastic behavior but still appears slightly anomalous. We will find below that the rate of angular momentum transfer between the bar and the halo is slightly slower for the multi-mass run. The multi-mass run seems to transport about 10% less angular momentum from the bar to the halo than the other runs and this could account for the different behavior.

Finally, we compare the pattern speed evolution of simulations at different resolutions. Figure 18 shows the pattern speed versus time for all simulations where again for a proper comparison we have synchronized the various runs to the time of the first peak in  $|A_2|$  as before. The decline of the pattern speed is similar for all resolutions with bars initially forming with  $\Omega_b \approx 35 \text{ km s}^{-1} \text{ kpc}^{-1}$  and ending with a value around  $\Omega_b \approx 12 - 14 \text{ km s}^{-1} \text{ kpc}^{-1}$ . The range of curves is again consistent with the scatter seen in the fixed resolution study. The highest resolution runs with 100M halo particles in both the single mass and multi-mass case show an apparent oscillation in  $\Omega_b$  during the decline. The frequency of this oscillation is approximately half of the pattern speed  $\Omega_b$  itself. The source of the oscillation is not obvious. We initially speculated that interference from spiral patterns beyond the end of the bar rotating at a different pattern speed may have altered the measurement of  $A_2$  within  $R < 0.5$ . However, when the pattern speed is derived from  $A_2$  measured within  $R < 0.25$  out of influence of spirals the oscillations persist at the same frequency. These oscillations may result from uneven bar growth (i.e., variations in length) by trapping of the disk orbits by the bar or from a non-linear mode coupling (Martinez-Valpuesta et al. 2006;

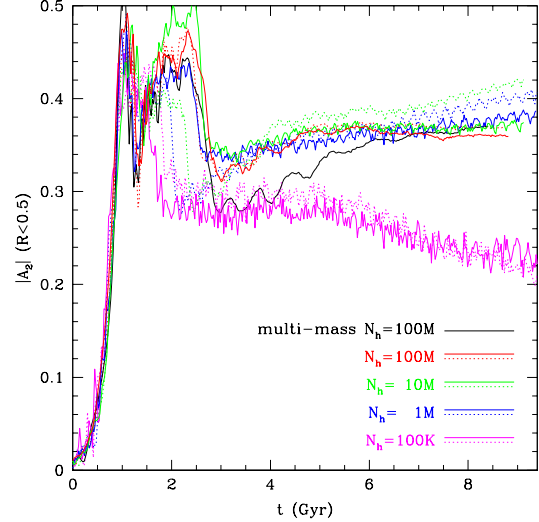


FIG. 17.— Evolution of the bar strength  $|A_2|$  for stars with  $R < 0.5$  for two model sequences using  $N_d = 18K, 180K, 1.8M, 18M$  with  $N_h = 100K, 1M, 10M, 100M$  respectively and the multi-mass model plotted versus linear time. The curves have been synchronized to the time of maximum bar extent. This plot emphasizes the variance in behavior after the bar instability goes nonlinear.

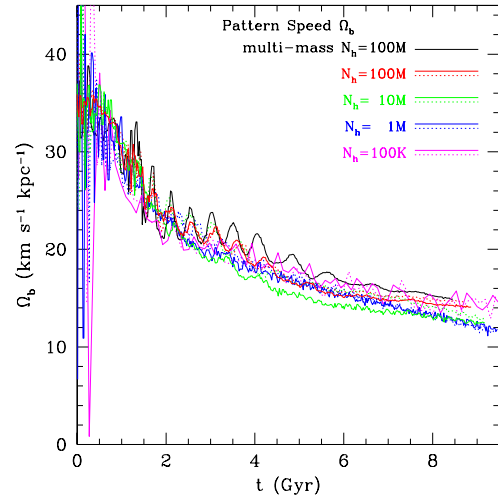


FIG. 18.— Evolution of the pattern speed  $\Omega_b$  for two model sequences using  $N_d = 18K, 180K, 1.8M, 18M$  with  $N_h = 100K, 1M, 10M, 100M$  respectively ( $R < 0.5$ ). Also, shown is one model with  $N_d = 18M$  and  $N_h = 100M$  with a multi-mass halo that increases the particle number density near the center of the disk. The curves have been shifted in time so that the bar growth evolution is coincident with the m1M model. The decline in pattern speed at different resolutions is similar though the multi-mass model does not decay as quickly and has a slightly larger pattern speed at the last simulated point. The 100M particle simulations also show a modulation of the pattern speed that indicates more subtle dynamical effects revealed by higher resolution.

Martinez-Valpuesta 2006).

In summary, the bar develops from Poisson noise in the disks in a similar way for simulations with  $N_h > 10^6$ . The time delay in the growth to the nonlinear phase for larger  $N_h$  are the result of smaller amplitude Poisson fluctuations that seed the bar at higher resolution. The



variation in the behavior of the different runs is consistent with the variance introduced from different random realizations of the models. The bar pattern speed decays at a similar rate over the course of the run for resolutions again with  $N > 10^6$  though the higher resolution runs decay to a final value that is approximately 10% larger. There is no dramatic change in dynamical evolution of gross physical properties of the bar as we approach  $N_h = 10^8$  suggesting the models are converging to the correct physical behavior.

### 3.4. A Fast Bar

Orbital dynamics permits a bar of length  $a_b$  to extend as far as the CR radius  $D_L$  (Contopoulos 1980). But the developing chaos between the Ultra-Harmonic resonance (UHR) and the CR limits the bar length to within the UHR, especially in stronger bars. The dimensionless ratio  $\mathcal{R} = D_L/a_b$  is an indicator of a bar's dynamical state and galaxies with observed or inferred pattern speeds have  $\mathcal{R} = 1.2 \pm 0.2$  (e.g., Athanassoula 1992; Debattista & Sellwood 1998). Bars emerging from the disk instability are usually born with  $\mathcal{R} \approx 1$  and this value gradually increases as the bar settles into equilibrium and loses angular momentum to the halo through dynamical friction. During buckling the bar shortens dramatically for some period of time (Martinez-Valpuesta & Shlosman 2004; Martinez-Valpuesta et al. 2006) and afterwards gradually lengthens. However, the CR radius also increases in response to the change in potential of both the outer disk and DM halo as they absorb angular momentum from the bar and respond to the changing mass profile of the disk. Debattista & Sellwood (2000) have shown that in many models with dense halos, bars are slowed down considerably and end up with values of  $\mathcal{R} > 2$ . Bars are, designated as “fast” if  $1 < \mathcal{R} < 1.4$  or “slow” for  $\mathcal{R} > 1.4$  with all barred galaxies with determined or inferred pattern speeds being “fast” by this definition.

The bar that forms in the model described here is “fast” with  $\mathcal{R} \lesssim 1.4$  after reaching a quasi-equilibrium after buckling. The result is in agreement with Martinez-Valpuesta et al. (2006) who used a similar galactic model and determined the bar size by means of the last stable orbit supporting it. At various times after the bar forms, we have determined the curve of the circular orbital frequency  $\Omega(R)$  by computing the average of the radial acceleration  $d\Phi/dR$  on points on rings of different radii in the midplane of the disk. In this way, we average out the asymmetry in the potential introduced by the bar. The CR radius is then found by reading off the radius corresponding to  $\Omega(D_L) = \Omega_b$  at the given time. To determine the bar length  $a_b$  we fit elliptical contours to the surface density profile and look for a sudden transition in the value of the axis ratio  $q = b/a$  and the position angle of the isodensity contours. In most cases, the transition is sudden, jumping from  $q = 0.4$  to  $q = 0.9$  over a radial interval of 1 kpc. We therefore can determine  $a_b$  with an accuracy of  $\pm 0.5$  kpc. Figure 19 shows the isodensity contours overlayed with corotation radius and elliptical contour for the chosen bar radius at  $t = 9.4$  Gyr the final time in the simulation for the highest resolution model mm100M. Even at this time, the bar nearly extends to the CR radius and  $\mathcal{R} = 1.2 \pm 0.05$ . Figure 20 shows the evolution of  $\mathcal{R}$  from  $t = 4.7$ –9.4 Gyr

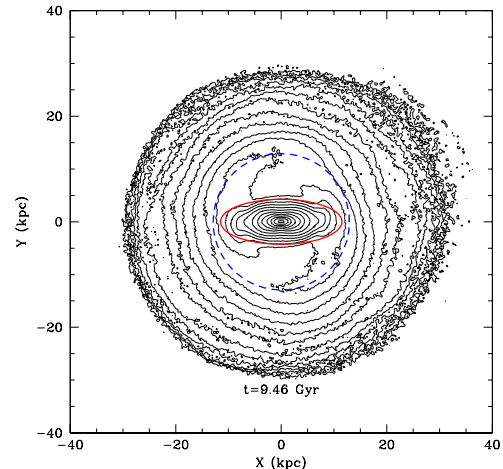


FIG. 19.— Surface brightness contours of the multi-mass model at the last snapshot at  $t = 9.4$  Gyr overlayed with the best fit ellipse to the central bar and co-rotation radius. Even at this late time in the evolution, the bar extends to the co-rotation radius.

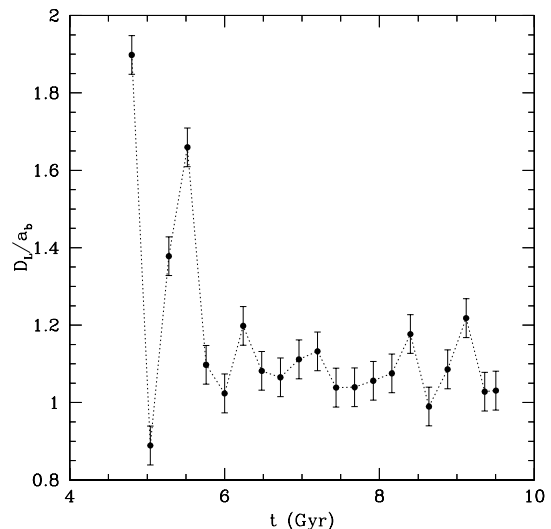


FIG. 20.— Evolution of the CR radius to bar length ratio  $\mathcal{R}$  for the multi-mass model over the last half of the simulation. The value of  $\mathcal{R}$  hovers around 1.1 indicating a fast bar.

starting with the time when it just has settled into equilibrium until the end of the run. During this time, the bar ratio  $\mathcal{R}$  maintains a value less than 1.4 and so would be classified as a “fast” bar and remain consistent with the observed barred galaxies. Despite a 3-fold drop in the pattern speed the bar length and the galaxy potential readjusts to keep  $\mathcal{R}$  near 1. (Debattista & Sellwood 2000) found that models with  $V_{\text{disk}}^2/V_{\text{halo}}^2 = 1$  do end up with fast bars and indeed our model is consistent with that value (Fig. 1).

Finally, we estimate the bar mass and shape for comparison to current studies on bar-halo interactions. The best fit ellipsoid to the bar with  $a_b = 12.5$  kpc has axis ratio  $a_1 : a_2 : a_3 = 3.6 : 1.4 : 1$ . The mass in the disk within the elliptical contour of  $q = 0.4$  with bar length

$a_b = 12.5$  kpc is  $M_b = 3.7 \times 10^{10} M_\odot$  compared with a total disk mass of  $M_d = 5.5 \times 10^{10} M_\odot$ . The bar therefore represents 2/3 of the total disk mass. The mass of the DM halo within the sphere of radius  $a_b = 12.5$  kpc is  $M_h(r < a_b) = 6.1 \times 10^{10} M_\odot$  compared with a total halo mass  $M_{h,tot} = 3.0 \times 10^{11} M_\odot$ . The ratio of bar to total halo mass enclosed is  $M_b/M_h(r < a_b) \sim 0.6$ . We will see below that this perturbation has a small effect on the density profile of the DM halo and is not sufficient to create a flat density core as seen in recent work with a rigid bar evolving in a spherical  $N$ -body halo with  $M_b/M_h = 0.5 - 1.0$  and a thinner bar with  $a_1 : a_2 : a_3 = 10 : 2 : 1$  (Weinberg & Katz 2007b).

#### 4. HALO DENSITY PROFILE EVOLUTION

Our next task is to examine the evolution of the dark halo density profile. Weinberg & Katz (2002) originally demonstrated that a thin *rigid* bar rotating within a cuspy dark halo can disturb the central density profile and set up a constant density core and follow-up work with improved methods and resolution confirmed that result for their particular choice of bar parameters (Weinberg & Katz 2007b). Sellwood (2008) has recently verified these results using independent methods but has questioned the applicability of the results of the dynamics of an idealized thin, rigid bar to real barred galaxies. The model described here differs from these studies by examining a *self-consistent model* of a bar forming from an instability in an exponential disk within a cusped dark halo and so arguably represents a system closer to reality. A detailed characterization of the model here will allow us to compare our results to these other studies.

Figure 21 presents the evolution of the density profile as a function of mass resolution. The plots show the profiles at changing times along with the differential change with respect to the initial profile. Gravitational softening introduces an artificial density core within  $\sim 3$  Plummer softening lengths but beyond this radius the plots clearly show similar behavior in the density profiles. A comparison of the final density profiles at different resolutions again shows similar behavior beyond the softening radius and convergence to a similar central behavior. The central density profile actually increases by  $1.7\times$  while maintaining a central cusp (Fig. 22). The likely cause of this increase is the halo response to the forming bar (Sellwood 2003; Colín et al. 2006). Once the bar buckles it forms a more concentrated mass distribution in the center of the disk and the halo responds by contracting adiabatically. In the multi-mass halo with  $N_h = 10^8$ , the density cusp is present down to  $r \approx 100$  pc where gravitational softening effects start to influence the dynamics. Within this radius, the halo is well-sampled by more than 6000 particles and flattens out into a constant density core dominated by softened gravity.

Weinberg & Katz (2007b) (WK herein) have recently shown that massive bars can decrease the central density of DM halos and disrupt the cusp over a Hubble time in some cases at radii of about 20% of the bar length. Our bar has a length  $a_b = 12.5$  kpc so we should expect to see distortions of the density profile at  $r \approx 2$  kpc while in fact we see no signs of a density core developing until softened gravity dominates at  $r = 0.1$  kpc in our highest resolution case. The results presented here seem to be in contradiction so what's going on? The reasons for dis-

agreement can be understood by comparing the detailed properties of the bars used in their models to our self-consistently evolved  $N$ -body bar. The WK models are rigid, homogeneous ellipsoids of various masses, lengths and axis ratios rotating within a live, isotropic  $N$ -body halo. Their fiducial model which strongly modifies the halo inner profile has a bar length equal to the NFW halo scale radius  $r_s$ , i.e.,  $a_b/r_s = 1.0$ , a bar mass equal to half the halo mass within this radius  $M_b/M_h = 0.5$  and an axis ratio  $a_1 : a_2 : a_3 = 10 : 2 : 1$ . Our halo is also NFW-like but not precisely a NFW model due to modifications introduced in setting it up with an embedded disk and changes induced by bar formation. A good proxy for  $r_s$  in our models is the radius  $r_{-2}$  where the density power-law slope  $\gamma = d \log \rho / d \log r \approx -2$  (For an NFW model  $\gamma = -2$  at  $r = r_s$ ). Figure 22 shows that  $r_{-2} \approx 3$  kpc initially. At late times, the  $\gamma$  profile develops a wiggle so that  $\gamma = -2$  occurs at two different radii, but the average of these two radii is  $r_s \approx 5$  kpc. The final bar length is about 12 kpc (Fig. 19) and so  $a_b/r_{-2} = 2.4$ . The  $N$ -body bar axis ratio measured above is  $a_1 : a_2 : a_3 = 3.6 : 1.4 : 1$  considerably fatter than the fiducial model of WK. Finally, the bar-to-halo mass ratio within the bar length is  $M_b/M_h = 0.6$ . The main differences between the WK fiducial model and our model is that their halo is more extended and the bar is much thinner overall while the mass ratios are comparable. The WK models with thicker bars with  $a_2/a_1 > 0.3$  are the closest ones to our  $N$ -body models and according to their Fig. 13 in Weinberg & Katz (2007b) cause no appreciable change in the density profile. So we find no inconsistency with their most closely matching model.

While the thin, massive bars described by WK have strong effects on halo profiles, the thicker bars that develop through the recurrent buckling instabilities are more relevant to the evolution of real barred galaxies. Thin bars are subject to the dynamical buckling instability and thicken quickly. Moreover, the strongest bars, i.e., those with  $b/a \sim 0.2$  show a rapid decrease in the phase space available to regular orbits and hence an increase in the fraction of chaotic orbits in the bar (Martinez-Valpuesta & Shlosman 2004). While vertically thin *rigid* bars are immune to any instabilities, the DM particle orbits in the cusp can be destabilized by the mere presence of a more massive analytical potential mixed with the live potential. Vertically thinner bars, i.e., smaller  $c/a$ , will be more efficient in destabilizing the DM trajectories, by analogy with smaller  $b/a$ . In any case, the  $c/a = 0.1$  thin bars used by WK cannot be justified over a Hubble time. They are supported neither by observations or high-resolution numerical simulations.

We conclude that bars that form self-consistently in  $N$ -body simulations from the instability of an exponential disk in NFW-like DM halos do not destroy the density cusp and in fact can increase the halo central density slightly. Our mass resolution study shows a clear convergence in behavior to higher resolution and the central characteristics of dark halos are limited only by the particle softening and diminishing particle numbers. We now explore the detailed orbital dynamics of the bars to understand angular momentum transport from the bar to the halo through low order resonances.

#### 5. BAR ORBITAL DYNAMICS

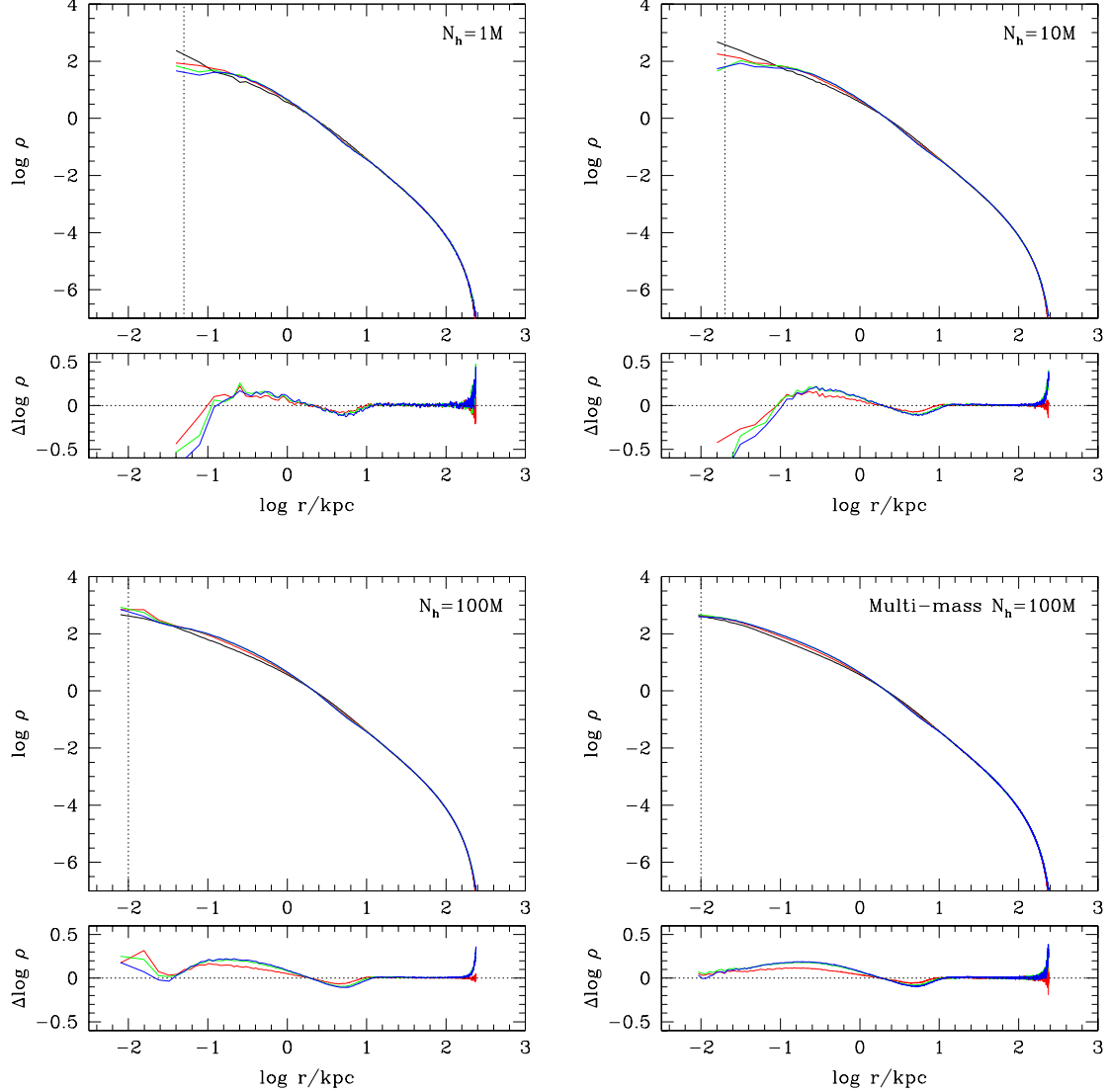


FIG. 21.— Evolution of the dark halo density profile for different mass resolutions at  $t = 0, 2.4, 4.7$  and  $7.1$  Gyr (black, red, green and blue lines). The dotted vertical line shows the value of the Plummer softening length for each resolution:  $\epsilon = 50, 20, 10$  and  $10$  pc for  $N_h = 10^6, 10^7, 10^8$  and  $10^8$  (multi-mass) halo models respectively. For  $r > 10$  kpc, the density profile does not change significantly. In the range  $1 < r < 10$  kpc, the density increases roughly  $1.7\times$ , showing adiabatic contraction in response to the buckling instability and the formation of a centrally concentrated bulge-like bar within the disk. The logarithmic slope of the density profile is  $\alpha \sim -1$  to within a few softening lengths from the center. A constant density core develops within the center with a core radius that depends on  $N_h$  and  $\epsilon$  with typical values of  $\sim 5\epsilon$ . As  $N_h$  increases and  $\epsilon$  decreases, central density increases while the core radius declines. The existence of a small core is consistent with relaxation due to softened gravity rather than forcing by the bar.

Angular momentum is transferred from the bar to the halo through low order orbital resonances (Lynden-Bell & Kalnajs 1972; Tremaine & Weinberg 1984; Weinberg 1985). Following the convention of Weinberg & Katz (2007a), the condition for planar resonances is  $l_1\Omega_r + l_2\Omega_\phi = m\Omega_b$  where  $(l_1, l_2, m)$  are an integer triplet with radial and azimuthal orbital frequencies  $\Omega_r$  and  $\Omega_\phi$  and bar pattern speed  $\Omega_b$  (Athanasoula 2002; Weinberg & Katz 2007a). In the discussion below, we also use the parameters  $\Omega \equiv \Omega_\phi$  and  $\kappa \equiv \Omega_r$  to refer to the true orbital frequencies rather than the epicyclic approximations. Bars are predominantly a  $m = 2$  disturbance so integer pairs  $l_1 : l_2$  with  $m = 2$  correspond to various resonances with the more important ones being the inner and outer Lindblad resonances (ILR  $-1 : 2$  and

OLR  $1 : 2$ ) and the corotation resonance (COR  $0 : 2$ ). Other important resonances that may transfer angular momentum occur with  $l_2 = -2, 0$  including the direct radial resonance (DRR  $1:0$ ) discussed by WK.

We focus our analysis on resonances with  $l_2 = 2$  that are responsible for the bulk of angular momentum transfer. A simple way of characterizing the low order resonances is with the dimensionless frequency  $\eta = (\Omega - \Omega_b)/\kappa$  (Athanasoula 2002; Martinez-Valpuesta et al. 2006). The half integer values of  $\eta$  correspond to low order resonances with  $\eta = -1/2, 0, 1/2$  corresponding to the OLR, COR, and ILR respectively. Most angular momentum is transferred to and from orbits that satisfy this resonant condition. As the bar loses angular momentum and  $\Omega_b$  declines, the population of halo particles in res-



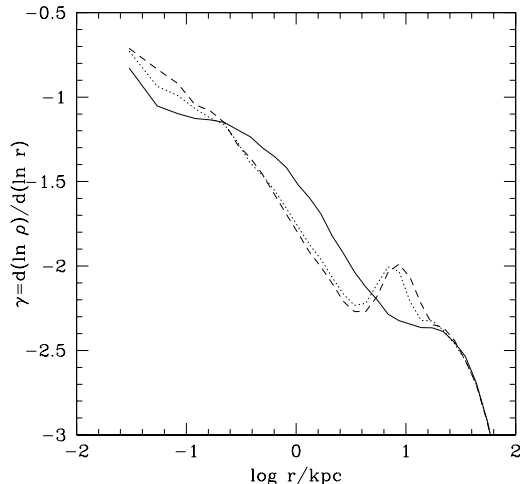


FIG. 22.— Change in the density power-law index profile  $\gamma = d \log \rho / d \log r$  at  $t = 0$  Gyr (solid), 4.7 Gyr (dotted) and 7.1 Gyr (dashed). The density profile maintains a cusped profile with  $\gamma < -1$  down to  $r = 0.1$  kpc well within the the scale radius,  $r_{-2} \approx 5$  kpc at late times. A constant density core does not develop in response to the bar and the halo maintains its cusp to the limit of gravitational softening.

onance with the bar changes. The potential of the halo also readjusts in response to the bar, so orbital frequencies can change as well. Weinberg & Katz (2007a) have argued that the resonances may only occur over a small fraction of the halo mass so that poorly resolved halos may not have sufficient numbers of particles to absorb angular momentum. Furthermore, noise in lower resolution simulations can cause particles to move in and out of resonance in a diffusive manner leading to an incorrect determination of angular momentum transfer. They estimate that as many as  $10^8$  halo particles are necessary to both populate resonances and suppress noise to converge on the correct behavior. We examine these effects directly at different resolutions by studying the behavior of angular momentum transfer and orbital resonances using our models at the recommended mass resolution and see if the results do converge.

### 5.1. Net Angular Momentum Transfer

We first examine the net angular momentum transfer evolution as a function of mass resolution (Fig. 24). We have again offset the times at different resolution so that they are synchronized with the time of maximum  $|A_2|$ . The initial behavior is similar though there is no clear trend in behavior between resolutions from  $t = 2.4 - 7.2$  Gyr reflecting the variance from different random initial conditions. At late times, however, the rate of angular momentum transfer from the bar to the halo depends on resolution, with lower resolution simulations transferring  $J$  more quickly than the highest resolution case. From  $t = 7.2 - 9.4$  Gyr the rate of change  $J$  is about two times larger for  $N_h = 1M$  than  $N_h = 100M$ . This effect could be the result of noise broadening the resonant interaction though this interpretation is complicated by the variance in behavior due to different initial conditions. In summary, there is a measurable difference in angular momentum transfer between high and low resolution

with the lowest resolution model transferring about 10% more angular momentum.

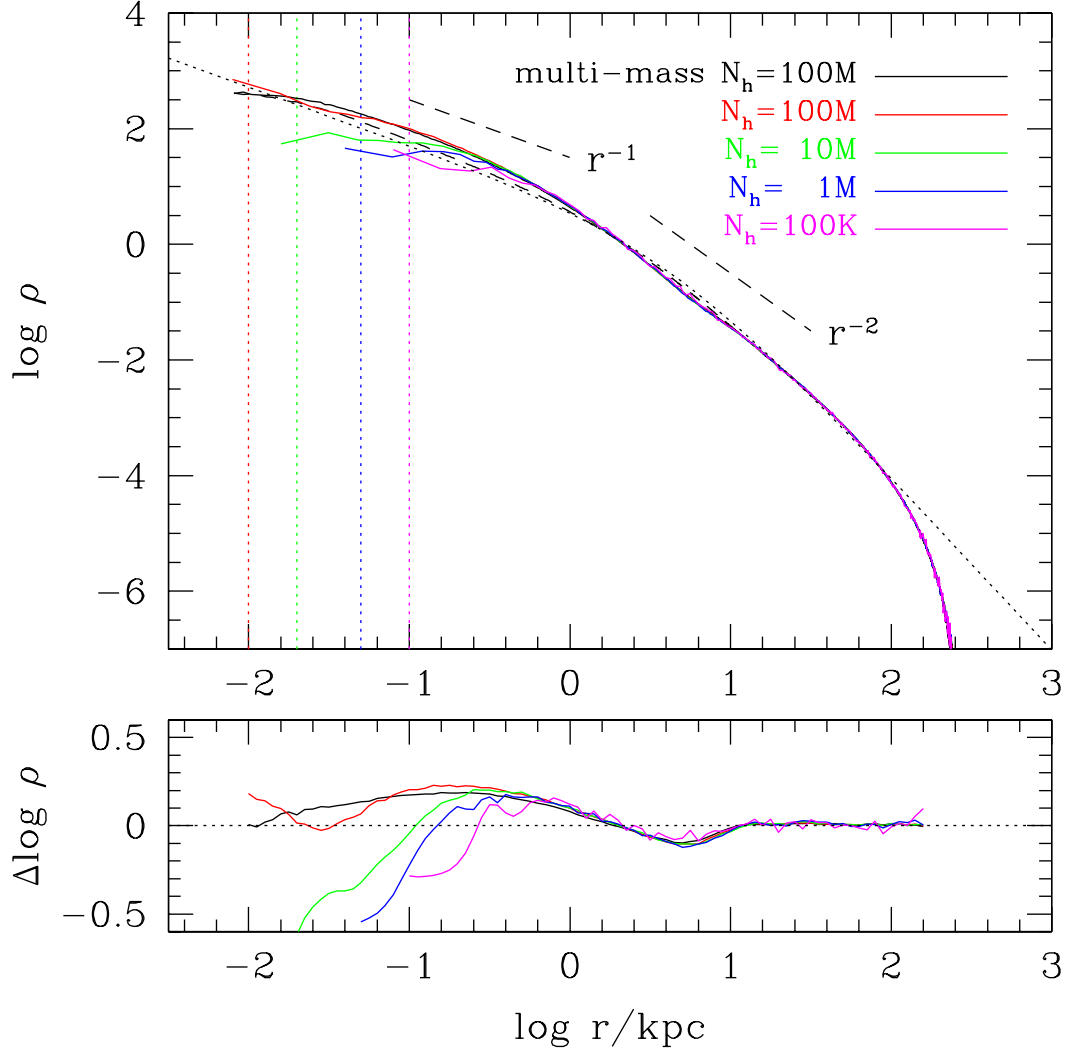


FIG. 23.— A comparison of density profiles at  $t = 7.1$  Gyr for different halo particle numbers  $N_h$ . We also show the initial density profile (dashed line) and the best fit NFW model curve (dotted line) to the initial profile over the range  $0 < r < 100$  kpc. The NFW parameters for the fit are  $r_s = 4.3$  kpc,  $v_{max} = 160$  km s $^{-1}$ , where  $v_{max}$  is the maximum circular velocity at  $r = 2.16r_s = 9.3$  kpc. Note that this halo is more concentrated than the typical galactic dark matter halos in cosmological simulations. We use the NFW formula to characterize the profile and show that an  $r^{-1}$  cusp extends to within at least 100 pc of the center. The dotted vertical lines show the softening length  $\epsilon$  used at different resolutions. As  $N_h$  increases, the central density increases and the core radius decreases suggesting that the core behavior is due to mass resolution rather than forcing by the bar.

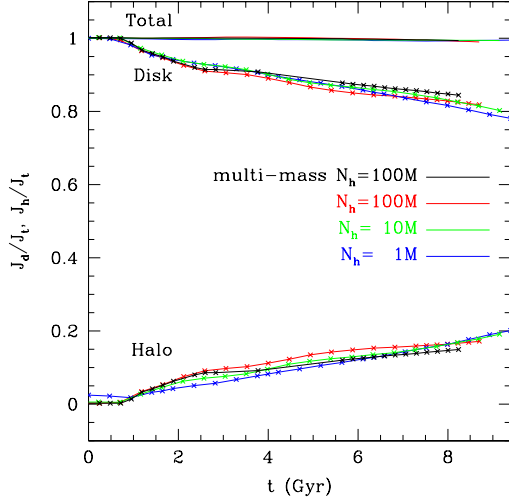


FIG. 24.— Evolution of the net angular momentum in the disk and halo at different mass resolution. Total angular momentum is conserved to within 1%. The evolution is similar for all resolutions plotted starting at  $N_h = 10^6$ . The rate of angular momentum transfer is slightly smaller at later times for higher resolution simulations leading to about a 10% difference in the total amount of transferred angular momentum in the multi-mass case suggesting a significant but small affect due to resolution.

### 5.2. Halo Orbital Resonances

We quantify the importance of low order resonances for angular momentum transfer in our models using a modified version of the orbital spectral analysis method (Binney & Spergel 1982) in a frozen rotating potential as described by Athanassoula (2002) and Martinez-Valpuesta et al. (2006). We determine the principal orbital frequencies  $\kappa$  and  $\Omega_\phi$  for a set of  $N_{Rh}$  randomly chosen particles in the halo with  $N_{Rh} \sim 10^6$  for simulations with  $N_h \geq 10^6$  and  $N_{Rh} = N_h$  for smaller simulations. We then compute the potential and force field on a grid with variable spacing to be used for interpolating forces for test particle integrations. Orbital frequencies are determined from test particle integration of particles orbits in the frozen potential in a rotating frame at the bar’s pattern speed for the time of a given snapshot. The orbits are integrated for about 50 bar rotations, starting at three representative times —  $t = 2.4, 4.7$  and  $7.1$  Gyr for the  $N_h = 10^8$  single and multi mass simulations. Appropriate time offsets are applied as discussed above to lower  $N_h$  simulations to synchronize the time of maximum  $|A_2|$ . Each orbit was sampled with at least 200 constant timesteps per azimuthal period, and overall by 10K timesteps. The use of constant timesteps simplifies Fourier decomposition of the orbit time series. Most decompositions lead to a line spectrum allowing easy identification of frequencies  $\Omega$  and  $\kappa$  though occasionally the spectrum is more complex and no frequencies can be uniquely identified.

We present the results of the spectral analysis for DM halo orbits in Fig. 25 for various resolutions at  $t = 7.1$  Gyr for the 100M particle runs. Again, we account for the time offsets discussed above for the lower resolution runs for a fair comparison. The particles are binned in frequency  $\eta$  with a bin width  $\Delta\eta = 0.005$ . Figure 25 shows the distribution of the particle number fraction

(or mass fraction in the multi-mass model case) as a function of the dimensionless frequency. The main resonances – ILR, COR, OLR – are present along with higher order ones with COR being the most populated resonance. The relative height of the peaks begins to converge when  $N > 10^6$  and the behavior is quite similar. The peak bins contain a few percent of the total particle numbers or  $\sim 10^6$  particles in the largest case and so provide good coverage of the resonance for angular momentum transfer. We can define the amount of mass in “resonance” as the sum over particles with dimensionless frequencies in the range  $\delta\eta \pm 0.05$  at half integer values of  $\eta$ . When measured this way about 7% of the total halo mass is in resonance instantaneously at late times when the bar has reached quasi-equilibrium and is slowing down. Tremaine & Weinberg (1984) speculated that orbits may have become trapped in resonance if the bar slowed down gradually and we can check whether this trapping is significant. A comparison of the particles in resonant peaks at  $t = 4.7$  Gyr with those at  $t = 7.1$  Gyr shows that only a small fraction migrate between resonances as the system evolves. Of the 7% of the total mass in resonance at  $t = 4.7$  Gyr only 1.5% are still in resonances at  $t = 7.1$  Gyr with most particles moving out of resonance. As the bar is braking, new orbits are brought into resonance while orbits that have acquired angular momentum move out of resonance. In this sense, the resonance is broad and a significant fraction of halo orbits participate in angular momentum exchange with the bar.

Figures 26 and 27 show the resonant transfer of angular momentum between the two snapshots at  $t = 4.7$  Gyr and  $t = 7.1$  Gyr. We plot the distribution of the change in z-angular momentum  $\Delta J_z$  versus  $\eta$  measured for the particles at  $t = 4.7$  Gyr. Most angular momentum is absorbed in the halo at the COR and OLR with smaller amounts absorbed at higher order resonances. However, some  $J_z$  is emitted and lost from the ILR in accord with fundamental ideas of angular momentum transport in stellar systems (Lynden-Bell & Kalnajs 1972). The distributions when viewed with an expanded vertical scale show nice convergence in detailed behavior at higher resolution (Fig. 27). For  $N_h > 10^7$ ,  $\approx 50\%$  of the total transferred angular momentum is in the resonant peaks (within  $\delta\eta = \pm 0.05$  while for  $N_h \leq 10^6$  we find less than 30% in the peaks with this same definition. The lower resolution simulations are clearly more susceptible to diffusion. Nevertheless, despite these differences the total angular momentum transferred is similar for  $N \geq 10^6$  suggesting that the diffusive process that broadens resonances is not a serious problem for the global evolution of the system.

### 5.3. Resonances in Phase Space

Finally, we examine the change in halo phase space density by computing the particle number density in  $(E, J_z)$  space and computing the difference between  $t = 0$  and  $t = 150$  in model m100M in a similar way to Holley-Bockelmann et al. (2005). In this way, we clearly see the resonant regions visible as discrete islands of particle overdensity in  $(E, J_z)$  space (Fig. 28). We can also overplot the values of  $(E, J_z)$  for the particles found in the resonant spikes in the analysis at the final time  $t = 150$  to see where they lie in phase space. Figure 29

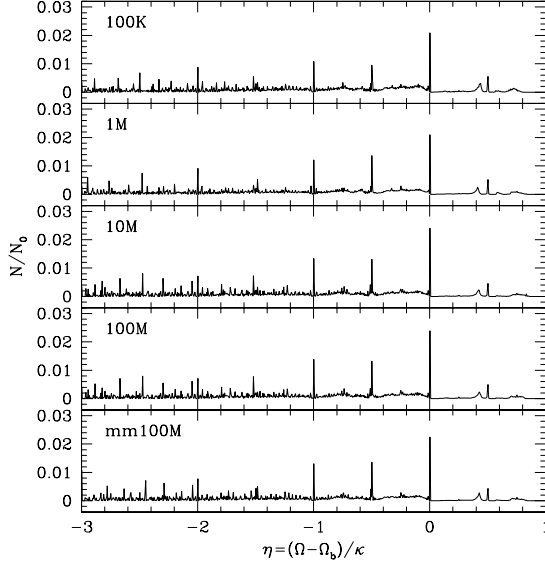


FIG. 25.— Distribution of DM halo particles as a function of the dimensionless frequency  $\eta$ . Resonant spikes at the half integer values of  $\eta$  correspond to low order resonances. The bin width is  $\delta\eta = 0.005$ . The distributions are similar as a function of mass resolution.

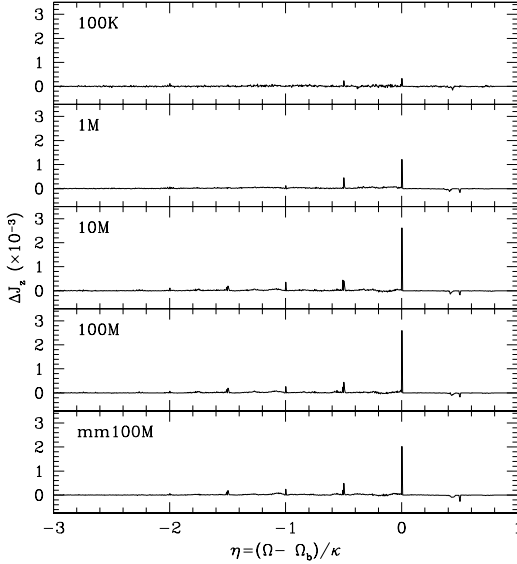


FIG. 26.— Net change in the DM halo particle angular momentum between  $t = 4.7$  and  $7.1$  Gyr for particles binned as a function of the dimensionless frequency  $\eta$  measured at  $t = 4.7$  Gyr. The majority of angular momentum is gained through the CR resonance at  $\eta = 0$  though some angular momentum is lost at the ILR at  $\eta = 0.5$ . The peaks are sharper at higher resolution.

clearly shows that the peaks in phase space density are directly related to the discrete resonances extracted from our spectral analysis. An accompanying animation to Fig 28 presents the time evolution of the differential number density in phase space and reveals how the resonant islands move through a large fraction of the halo mass. By counting particles in resonant peaks at different times we estimate that roughly 20-30% of the halo particles are

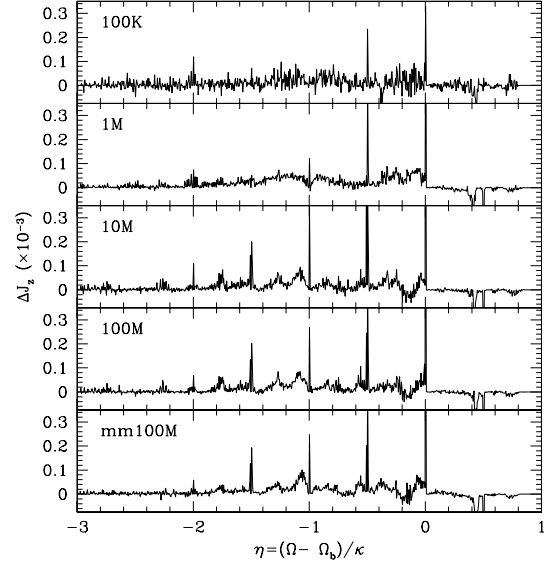


FIG. 27.— Same as Fig. 26 with the vertical scale expanded by  $10\times$ . The detailed distributions of the change in angular momentum are similar between the peaks at higher resolution.

in resonance with the bar at some time in their history. Since such a large fraction of particles are involved in angular momentum transfer then even lower resolution simulations can do a reasonable job of following the evolution of the bar.

## 6. CONCLUSIONS

We have carried out a comprehensive set of experiments to explore the evolution of a self-consistent bar in a galactic model with an exponential disk and cuspy DM halo using resolutions with  $10^4$ – $10^8$  DM particles and a single experiment using a multi-mass method with an effective resolution of  $10^{10}$ . Our highest resolution exceeds by far the level prescribed by Weinberg & Katz (2007a) necessary to achieve convergent behavior in bar galaxy dynamics. We have applied various diagnostics of bar evolution as a function of mass resolution including bar growth, pattern speed evolution, halo density cusp evolution and the resonant transfer of angular momentum from the bar to the DM halo. In almost all cases, the general behavior is similar at most but the lowest resolutions with the convergence occurring around  $10^6$ – $10^7$ , depending on the phenomenon. Sellwood (2008) has also explored similar effects in a mass resolution study with rigid bars in cuspy spherical halos with  $\sim 10^8$  particles and come to similar conclusions about minimal resolution requirements. Notably, in this model the density cusp is not destroyed by the formation of the bar in apparent contradiction to the results of WK. Our best explanation is that the thick bar that form in our self-consistent models has a weaker affect than the rigid thin bars in the work of WK and we question the applicability of these thin bar models over a Hubble time in light of the buckling instability.

The strongest argument for convergence comes from the spectral analysis of orbits in the rotating barred potential at different resolutions that shows in detail similar distributions as a function of the dimensionless frequency  $\eta$  both in mass fractions and angular momentum trans-

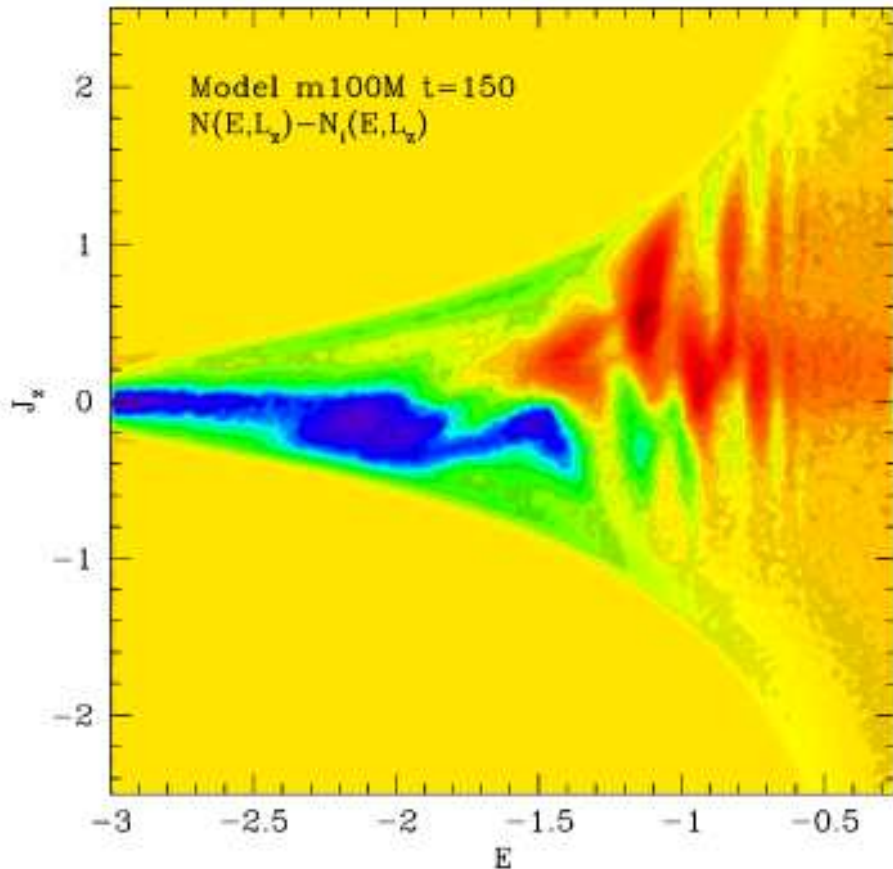


FIG. 28.— Change in particle number density in  $(E, J_z)$  space between  $t = 0$  and  $t = 150$  (7.0 Gyr) for the  $N_h = 10^8$  single mass model. The resonant regions show up clearly as peaks (red regions) in phase space in the left panel. The blue-black region is a valley where a halo bar rotating along with the disk bar and so de-populated the negative  $J_z$  of phase space at the ILR. See Video 4 to view the time evolution of the particle phase-space density.

ferred between different times. Analysis of the change in phase space density show that resonant islands sweep through the phase space as the bar loses angular momentum leading to effectively broader resonances with as much as 20-30% of the halo mass absorbing angular momentum from the bar.

Future studies should examine the bar instability self-consistently using the same initial conditions with different  $N$ -body methods to resolve current inconsistent results on the cusp/core evolution of DM halos as well as explore detailed behavior in phase space. The model snapshots and initial conditions from this study are freely available to researchers in the area who wish to verify our results against their own codes and methods.

We acknowledge useful discussions with Jerry Sellwood, Simon White, James Binney, Linda Sparke and Larry Widrow. We also thank the referee for useful comments. This work was supported, in part, by the NSERC of Canada and the Canadian Foundation for Innovation. I.S. acknowledges JILA Visiting Fellowship and partial support from NASA/ATP/LTSA, NSF and the STScI. I.B. acknowledges financial support from the Volkswagen Foundation (Ref: I/80 041-043). Supercomputing was provided by SHARCNET facilities at McMaster University and the University of Waterloo as well as facilities at CITA.

#### REFERENCES

- Athanassoula, E. 1992, *MNRAS*, 259, 328
- Athanassoula, E. 1996, in *Astronomical Society of the Pacific Conference Series*, Vol. 91, IAU Colloq. 157: Barred Galaxies, ed. R. Buta, D. A. Crocker, & B. G. Elmegreen, 309–+

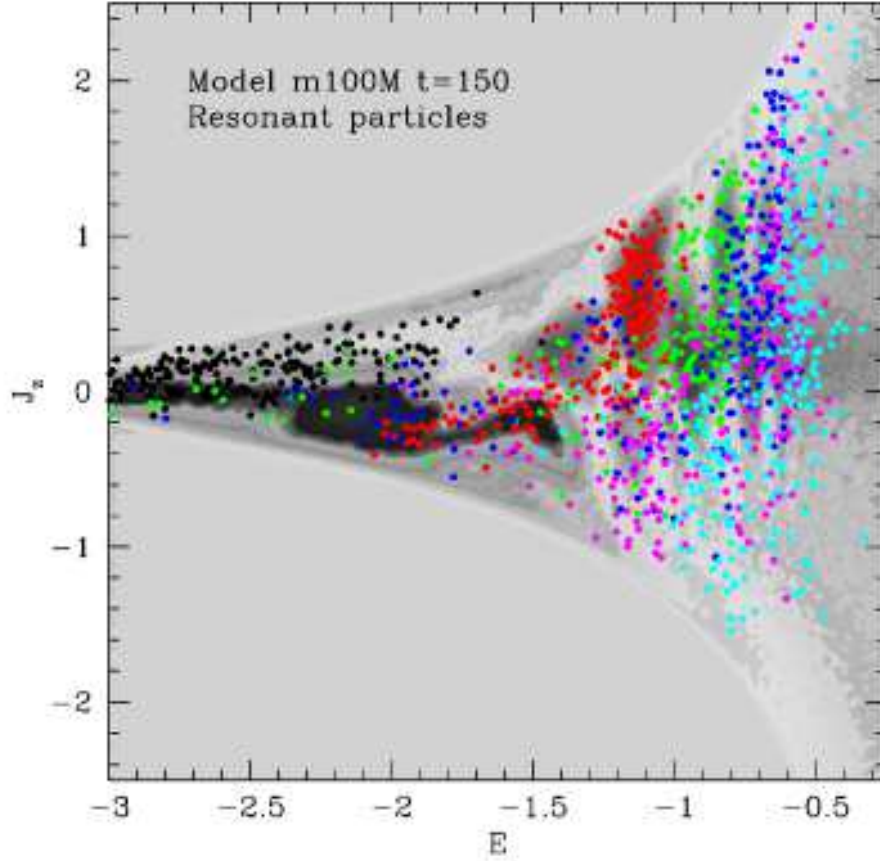


FIG. 29.— On the phase number density map, we overplot the  $(E, J_z)$  coordinates of a subset of particles located at discrete resonances at  $t = 150$  within  $\delta\eta = \pm 0.05$  (black-ILR- $\eta = 0.5$ , red-COR- $\eta = 0.0$ , green-OLR- $\eta = -0.5$ , blue- $\eta = -1.0$ , magenta- $\eta = -1.5$ , and cyan- $\eta = -2.0$ ). The resonant particles lay directly on top of the peaks and so identify the specific resonant regions in phase space.

- . 2002, *ApJ*, 569, L83  
 Berentzen, I., Heller, C. H., Shlosman, I., & Fricke, K. J. 1998, *MNRAS*, 300, 49  
 Binney, J., & Spergel, D. 1982, *ApJ*, 252, 308  
 Byrd, G. G., Valtonen, M. J., Valtaoja, L., & Sundelius, B. 1986, *A&A*, 166, 75  
 Ceverino, D., & Klypin, A. 2007, *MNRAS*, 379, 1155  
 Colín, P., Valenzuela, O., & Klypin, A. 2006, *ApJ*, 644, 687  
 Combes, F., Debbasch, F., Friedli, D., & Pfenniger, D. 1990, *A&A*, 233, 82  
 Combes, F., & Sanders, R. H. 1981, *A&A*, 96, 164  
 Contopoulos, G. 1980, *A&A*, 81, 198  
 Corsini, E. M., Aguerri, J. A. L., Debattista, V. P., Pizzella, A., Barazza, F. D., & Jerjen, H. 2007, *ApJ*, 659, L121  
 Debattista, V. P., Mayer, L., Carollo, C. M., Moore, B., Wadsley, J., & Quinn, T. 2006, *ApJ*, 645, 209  
 Debattista, V. P., & Sellwood, J. A. 1998, *ApJ*, 493, L5+  
 —. 2000, *ApJ*, 543, 704  
 Dubinski, J. 1996, *New Astronomy*, 1, 133  
 Dubinski, J., & Carlberg, R. G. 1991, *ApJ*, 378, 496  
 Dubinski, J., Gauthier, J.-R., Widrow, L., & Nickerson, S. 2008, *ArXiv e-prints*, 802  
 Gauthier, J.-R., Dubinski, J., & Widrow, L. M. 2006, *ApJ*, 653, 1180  
 Grobøl, P., Patsis, P. A., & Pompei, E. 2004, *A&A*, 423, 849  
 Hernquist, L., & Weinberg, M. D. 1992, *ApJ*, 400, 80  
 Holley-Bockelmann, K., Weinberg, M., & Katz, N. 2005, *MNRAS*, 363, 991  
 Jogee, S., Barazza, F. D., Rix, H.-W., Shlosman, I., Barden, M., Wolf, C., Davies, J., Heyer, I., Beckwith, S. V. W., Bell, E. F., Borch, A., Caldwell, J. A. R., Conselice, C. J., Dahlen, T., Häussler, B., Heymans, C., Jahnke, K., Knapen, J. H., Laine, S., Lubell, G. M., Mobasher, B., McIntosh, D. H., Meisenheimer, K., Peng, C. Y., Ravindranath, S., Sanchez, S. F., Somerville, R. S., & Wisotzki, L. 2004, *ApJ*, 615, L105  
 Kent, S. M. 1987, *AJ*, 93, 1062  
 Klypin, A., Valenzuela, O., Colin, P., & Quinn, T. 2008, *ArXiv e-prints*, 0808.3422  
 Knapen, J. H., Shlosman, I., & Peletier, R. F. 2000, *ApJ*, 529, 93  
 Kuijken, K., & Dubinski, J. 1995, *MNRAS*, 277, 1341  
 Lynden-Bell, D., & Kalnajs, A. J. 1972, *MNRAS*, 157, 1  
 Marinova, I., & Jogee, S. 2007, *ApJ*, 659, 1176  
 Martinez-Valpuesta, I. 2006, Ph.D. Thesis (University of Hertfordshire)  
 Martinez-Valpuesta, I., & Shlosman, I. 2004, *ApJ*, 613, L29  
 Martinez-Valpuesta, I., Shlosman, I., & Heller, C. 2006, *ApJ*, 637, 214  
 McMillan, P. J., & Dehnen, W. 2005, *MNRAS*, 363, 1205

- Merrifield, M. R., & Kuijken, K. 1995, MNRAS, 274, 933
- Navarro, J. F., Frenk, C. S., & White, S. D. M. 1996, ApJ, 462, 563
- Navarro, J. F., & Steinmetz, M. 2000, ApJ, 538, 477
- Noguchi, M. 1987, MNRAS, 228, 635
- O'Neill, J. K., & Dubinski, J. 2003, MNRAS, 346, 251
- Patsis, P. A., Skokos, C., & Athanassoula, E. 2002, MNRAS, 337, 578
- Raha, N., Sellwood, J. A., James, R. A., & Kahn, F. D. 1991, Nature, 352, 411
- Rautiainen, P., Salo, H., & Laurikainen, E. 2008, MNRAS, 760
- Romano-Diaz, E. and Shlosman, I., Heller, C., & Hoffman, Y. 2008, ApJ, submitted
- Sellwood, J. A. 1980, A&A, 89, 296
- . 2003, ApJ, 587, 638
- . 2008, ApJ, 679, 379
- Sellwood, J. A., & Wilkinson, A. 1993, Reports of Progress in Physics, 56, 173
- Sheth, K., Elmegreen, D. M., Elmegreen, B. G., Capak, P., Abraham, R. G., Athanassoula, E., Ellis, R. S., Mobasher, B., Salvato, M., Schinnerer, E., Scoville, N. Z., Spalsbury, L., Strubbe, L., Carollo, M., Rich, M., & West, A. A. 2008, ApJ, 675, 1141
- Shu, F. H. 1969, ApJ, 158, 505
- Sigurdsson, S., Hernquist, L., & Quinlan, G. D. 1995, ApJ, 446, 75
- Springel, V., Yoshida, N., & White, S. D. M. 2001, New Astronomy, 6, 79
- Toomre, A. 1981, in Structure and Evolution of Normal Galaxies, ed. S. M. Fall & D. Lynden-Bell, 111–136
- Tremaine, S., & Weinberg, M. D. 1984, MNRAS, 209, 729
- Valenzuela, O., & Klypin, A. 2003, MNRAS, 345, 406
- Weinberg, M. D. 1985, MNRAS, 213, 451
- Weinberg, M. D., & Katz, N. 2002, ApJ, 580, 627
- . 2007a, MNRAS, 375, 425
- . 2007b, MNRAS, 375, 460
- Widrow, L. M., & Dubinski, J. 2005, ApJ, 631, 838